

# Growth of Asteroids, Planetary Embryos and Kuiper Belt Objects by Chondrule Accretion

Anders Johansen<sup>1</sup>, Mordecai-Mark Mac Low<sup>2</sup>, Pedro Lacerda<sup>3</sup>, Martin Bizzarro<sup>4</sup>

<sup>1</sup>Lund Observatory, Department of Astronomy and Theoretical Physics, Lund University, Box 43, 22100 Lund, Sweden

<sup>2</sup>Department of Astrophysics, American Museum of Natural History, 79th Street at Central Park West, New York, NY 10024-5192, USA

<sup>3</sup>Max Planck Institute for Solar System Research, Justus-von-Liebig-Weg 3, 37077 Göttingen, Germany

<sup>4</sup>Centre for Star and Planet Formation and Natural History Museum of Denmark, University of Copenhagen, Øster Voldgade 5-7, 1350 Copenhagen, Denmark

## Abstract

Chondrules are millimeter-sized spherules that dominate primitive meteorites (chondrites) originating from the asteroid belt. The incorporation of chondrules into asteroidal bodies must be an important step in planet formation, but the mechanism is not understood. We show that the main growth of asteroids can result from gas-drag-assisted accretion of chondrules. The largest planetesimals of a population with a characteristic radius of 100 km undergo run-away accretion of chondrules within  $\sim 3$  Myr, forming planetary embryos up to Mars sizes along with smaller asteroids whose size distribution matches that of main belt asteroids. The aerodynamical accretion leads to size-sorting of chondrules consistent with chondrites. Accretion of mm-sized chondrules and ice particles drives the growth of planetesimals beyond the ice line as well, but the growth time increases above the disk life time outside of 25 AU. The contribution of direct planetesimal accretion to the growth of both asteroids and Kuiper belt objects is minor. In contrast, planetesimal accretion and chondrule accretion play more equal roles for the formation of Moon-sized embryos in the terrestrial planet formation region. These embryos are isolated from each other and accrete planetesimals only at a low rate. However, the continued accretion of chondrules destabilizes the oligarchic configuration and leads to the formation of Mars-sized embryos and terrestrial planets by a combination of direct chondrule accretion and giant impacts.

## Introduction

The formation of planetesimals and planetary embryos is an important step towards the assembly of planetary systems (1,2). The asteroid belt contains planetesimals left over from the formation of the solar system and thus provides a record of the early stages of planet formation. Chondrite meteorites are fragments of asteroids that did not undergo large-scale melting and differentiation. Their constituent particles allow us to study the first stage of planet formation, where micrometer-sized dust grains grew to asteroid-scale planetesimals. The dominant mass fraction of most chondrite meteorites are chondrules, millimeter-sized glassy spherules formed by transient heating events in the protoplanetary disk (3). The small matrix grains that fill the space between these chondrules likely entered the meteorite parent bodies as accretionary rims on the chondrules (4).

Uranium-corrected Pb-Pb dates of chondrules show crystallisation ages ranging from the earliest epoch of the solar protoplanetary disk – defined by the condensation of calcium-aluminium-rich inclusions (CAIs)  $4567.30 \pm 0.16$  Myr ago – to approximately 3 Myr later (5). Moreover, chondrules from individual chondrites show variability in their  $^{54}\text{Cr}/^{52}\text{Cr}$  and  $^{50}\text{Ti}/^{47}\text{Ti}$  ratios (5, 6) that track genetic relationships between early-formed solids and their respective reservoirs. Collectively, these observations indicate that chondrules from individual chondrite groups formed in different regions of the protoplanetary disk and were subsequently transported to the accre-

tion regions of their respective parent bodies. Thus, the region of asteroid formation must have been dominated by chondrules over time-scales comparable to the observed lifetimes of protoplanetary disks around young stars (7).

Meteorites provide a direct view of the primitive, chondritic material from which the planetesimals in the asteroid belt formed. In contrast, planetesimals originally located in the formation region of terrestrial planets accreted into planetary bodies and hence little evidence exists with respect to the material from which those planetesimals formed. However, the abundance of chondrules in the asteroid belt suggests that chondrules could have been widespread in the terrestrial planet formation region as well. Indeed, some chondrules record  $^{54}\text{Cr}/^{52}\text{Cr}$  and  $^{50}\text{Ti}/^{47}\text{Ti}$  ratios indicating formation in the accretion regions of Earth and Mars (5, 6). Hence, understanding the role of chondrules in the formation of asteroids can provide critical insights into how the terrestrial planets formed closer to the Sun.

The mechanism by which large amounts of chondrules were incorporated into asteroids is poorly understood. Particles of chondrule sizes can concentrate near the smallest scales of the turbulent gas (8). The most extreme concentration events have been proposed to lead to asteroid formation by gravitational contraction of such intermittent chondrule clouds (9). However, it is still debated whether such high concentrations actually occur (10). The streaming instability (11) is an alternative mechanism that concentrates larger particles (12, 13), of typical sizes from 10 cm to 1 m when applied to the asteroid belt, due

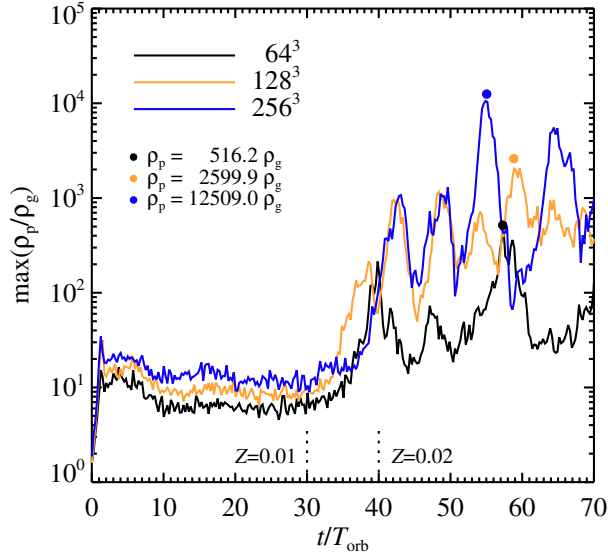


Figure 1: The maximum particle density versus time for streaming instability simulations without self-gravity at resolutions  $64^3$  (black line),  $128^3$  (yellow line) and  $256^3$  (blue line). The particle density is measured in units of the mid-plane gas density  $\rho_g$  and the time in units of the orbital period  $T_{\text{orb}}$ . The first 30 orbits are run with a solids-to-gas ratio of  $Z = 0.01$ , with only modest overdensities seen in the particle density. Half of the gas is then removed over the next 10 orbits, triggering strong particle concentration, of up to 10,000 times the local gas density at the highest resolution. Doubling the resolution leads to a more than a quadrupling of the maximum particle density.

to an aerodynamical effect where particles pile up in dense filaments, which can reach densities of more than 1,000 times the local gas density (14). The streaming instability nevertheless fails to concentrate chondrule-sized particles whose motion is strongly damped by gas drag (15).

## Results

Here we report the results of a model where asteroids and planetary embryos grow by accretion of chondrules onto planetesimal seeds formed by the streaming instability. Particles of large enough size to concentrate by streaming instabilities could have been present in the early stages of the protoplanetary disk when planetesimals formed. Such particles include macrochondrules (16), chondrule aggregates (17) and ice-rich pebbles. All of these drift rapidly towards the Sun because of gas drag. Therefore we assume that cm-sized particles were only present in the earliest stages of the protoplanetary disk, whereas smaller chondrules existed during most of the disk’s life-time. Chondrule-sized particles may have been able to remain in the asteroid belt due to stellar outflows (18) or advection with the outwards moving gas in the mid-plane layer of

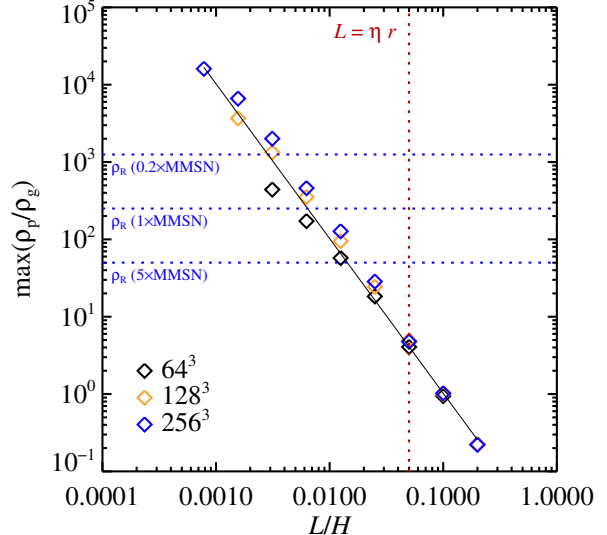


Figure 2: The maximum particle density versus the length scale (measured in scale-heights  $H$ ). We have taken spheres with diameters from one grid cell up to the largest scale of the simulation and noted the maximum value of the density over all simulation snapshots. The results are relatively converged on each scale. The increase in maximum particle density with increasing resolution is an effect of resolving ever smaller-scale filaments. Blue dotted lines mark the Roche density at three values of the gas column density at 2.5 AU compared to the Minimum Mass Solar Nebula (MMSN). The red dotted line indicates the characteristic length scale of the streaming instability. The black line shows a power law of slope  $-2$ , which shows that the maximum density follows approximately the inverse square of the length scale.

sedimented particles (15). We discuss the conditions for planetesimal formation in the asteroid belt, particularly the formation of dm-sized particles, further in the Supplementary Text.

## Planetesimal formation simulations

We use high-resolution models of planetesimal formation through streaming instabilities to set the initial conditions for our model. The highest resolution reached prior to this work in such simulations is  $128^3$  grid cells with 2.4 million superparticles representing the solids (14). We here report on simulations with up to  $512^3$  grid cells and 153.6 million superparticles representing the solids, which is 64 times more resolution elements than in previous simulations. Details of the simulation method are given in Materials and Methods.

We first perform a convergence test of streaming instability simulations with no self-gravity between the particles. Figure 1 shows the maximum particle density versus time in these simulations. We run the initial 30 orbits with the full gas density. Here the maximum particle density is very moderate and no

strong concentrations occur. Between 30 and 40 orbits we remove 50% of the gas, effectively increasing the solids-to-gas ratio from  $Z = 0.01$  to  $Z = 0.02$ . This increase in metallicity triggers strong particle concentration through the streaming instability, of up to 10,000 times the local gas density. The maximum particle density increases approximately quadratically with the inverse size of the resolution element  $\delta x$ . The maximum particle density on different scales is shown in Figure 2. Here we have measured the maximum density in spheres of diameters from  $\delta x$  up to the full size of the simulation box. The results are well converged from  $64^3$  to  $256^3$  at the scales that are present at all resolutions. The smaller scales made accessible at higher resolution yield increasingly higher densities. This is an effect of the filamentary structure of the overdense particle filaments forming by the streaming instability; higher resolution allows us to resolve finer structure and hence higher densities. Smaller planetesimals can thus form as the resolution is increased and increasingly smaller-scale filaments cross the Roche density.

In Figure 3 we show size distributions of planetesimals forming in streaming instability simulations that include the self-gravity of the particles. The planetesimal size distribution is dominated in number by small planetesimals, but most of the mass is in the few largest bodies. We find that progressively smaller planetesimals form, alongside the large planetesimals, at higher resolution. The largest planetesimals, which contain the dominant mass of the population, decrease to approximately 100 km in radius for the column density of the Minimum Mass Solar Nebula at the location of the asteroid belt (19). The size distribution of asteroids above 60 km in radius has been shown to retain its primordial shape, since the depletion of the asteroid belt happens in a size-independent fashion for those large bodies (20, 21). The differential size distribution resulting from streaming instabilities disagrees with the observed size distribution of the asteroids (dashed line in Figure 3).

### Chondrule accretion on asteroids

We proceed to consider the subsequent evolution of the size distribution as the newly formed planetesimals accrete chondrules present in the gaseous surroundings. We assume that planetesimals are born within an ocean of small chondrules that do not directly participate in planetesimal formation. Accretion of these chondrules by the planetesimals over the following millions of years can lead to significant mass growth. We use initial size distributions inspired by the streaming instability simulations. However, chondrule accretion is not limited to this model; it would be efficient in the context of any planetesimal formation mechanism that produces planetesimals with characteristic sizes of 100 km (9, 22).

The gas in the protoplanetary disk is slightly pressure-supported in the radial direction and hence moves at a sub-Keplerian speed, with  $\Delta v$  marking the difference between the Keplerian speed and the actual gas speed. The speed difference is approximately 53 m/s in the optically thin Minimum Mass Solar Nebula model (19). The Bondi radius of a planetesimal

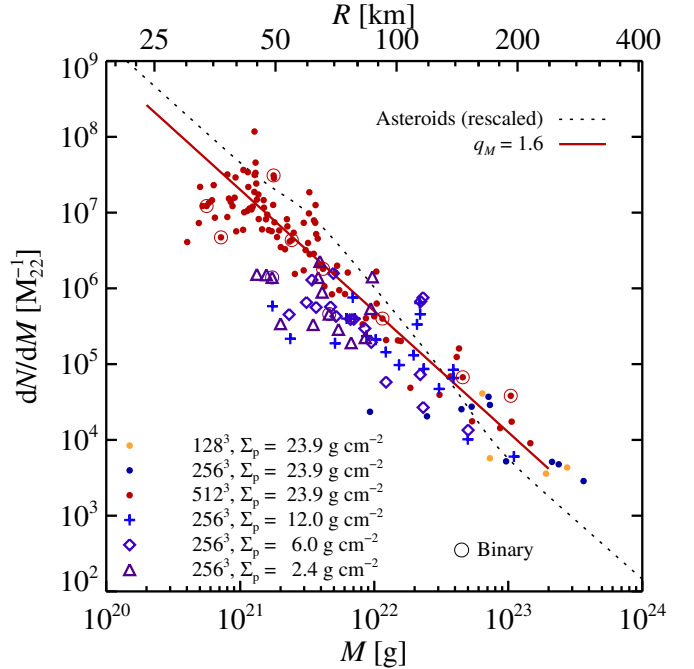


Figure 3: Birth size distribution of planetesimals forming by the streaming instability in 25-cm-sized particles. The differential number of planetesimals (per  $10^{22}$  g) is calculated with respect to the nearest size neighbours in the simulation. Yellow, blue and red circles indicate individual planetesimals forming in computer simulations at  $128^3$ ,  $256^3$  and  $512^3$  grid cells. The size distribution of the highest-resolution simulation is fitted well with a power law  $dN/dM \propto M^{-q_M}$  (red line; the fit is based on the cumulative size distribution shown in Figure 4, but does not include the exponential tapering). Simulations with lower values of the particle column density  $\Sigma_p$  yield successively smaller radii for the largest planetesimals, down to below 100 km in radius for a column density similar to the Minimum Mass Solar Nebula model ( $\Sigma_p = 4.3 \text{ g cm}^{-2}$  at  $r = 2.5 \text{ AU}$ ). Binary planetesimals (marked with circles) appear only in the highest-resolution simulation, as binary survival requires sufficient resolution of the Hill radius. The differential size distribution of the asteroid belt (dashed line) shows characteristic bumps at 60 km and 200 km. The planetesimal birth sizes from the simulations are clearly not in agreement with main belt asteroids.

with radius  $R$  and internal density  $\rho_\bullet$ ,

$$\frac{R_B}{R} = 3.5 \left( \frac{R}{100 \text{ km}} \right)^2 \left( \frac{\Delta v}{53 \text{ m/s}} \right)^{-2} \left( \frac{\rho_\bullet}{3.5 \text{ g/cm}^3} \right), \quad (1)$$

measures the gravitational deflection radius of the planetesimal. Chondrules embedded in the sub-Keplerian gas flow are accreted from the Bondi radius (23, 24) when their friction time  $t_f$  is comparable to the time to drift azimuthally across the Bondi

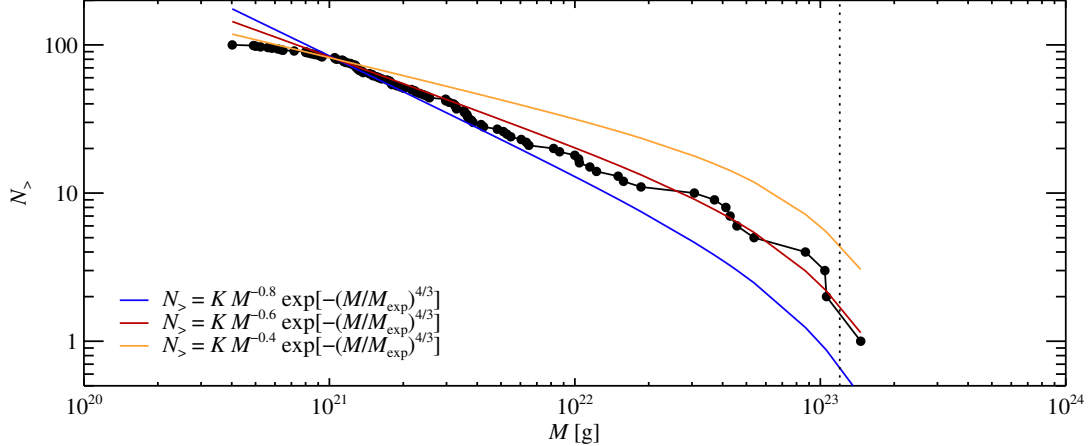


Figure 4: Cumulative birth size distribution of planetesimals forming by the streaming instability in our highest-resolution simulation ( $512^3$ ). The cumulative size distribution is fitted with an exponentially tapered power law  $N_{>} \propto M^{-0.6} \exp[-(M/M_{\text{exp}})^{4/3}]$  (red line), with exponential tapering at  $M_{\text{exp}} = 1.2 \times 10^{23}$  g (dotted line). Shallower or steeper power laws yield poorer fits to the populations of small and large planetesimals, respectively. We choose to fit the cumulative size distribution rather than the differential size distribution to avoid the noise inherently present in the latter. The fit can be translated to  $dN/dM \propto M^{-1.6} \exp[-(M/M_{\text{exp}})^{4/3}]$  (the power law part of this fit is indicated in Figure 3) as well as to  $dN/dR \propto R^{-2.8} \exp[-(R/R_{\text{exp}})^4]$  in the differential size distribution per unit radius.

radius,  $t_B = R_B/\Delta v$ . An additional turbulent component to the gas motion can be ignored since this is expected to be much slower than the sub-Keplerian speed in the asteroid formation region. Peak accretion rates are obtained for  $t_f/t_B$  in the range from 0.5 to 10 (24). This happens at the orbital distance of the asteroid belt for particle sizes in the interval

$$a = [0.08, 1.6] \text{ mm} \left( \frac{R}{100 \text{ km}} \right)^3 \left( \frac{\Delta v}{53 \text{ m/s}} \right)^{-3} f_{\text{gas}}. \quad (2)$$

Here  $f_{\text{gas}}$  represents the ratio of the actual gas column density to that of the Minimum Mass Solar Nebula (19). Chondrule accretion happens at a rate proportional to  $R_B^2$  (or  $\dot{M} \propto R^6$ ). This run-away accretion can drive a very steep differential size distribution similar to what is observed for large asteroids in the asteroid belt.

We solve numerically for the temporal evolution of the sizes and orbits of planetesimals accreting chondrules and colliding with each other in an annulus extending from 2.4 to 2.6 AU (see Materials and Methods for details). The planetesimals have initial radii from 10 to 150 km, distributed in size along an exponentially tapered power law based on the cumulative size distribution of planetesimals forming in the streaming instability simulations (see Figure 4),  $dN/dR \propto R^{-2.8} \exp[-(R/R_{\text{exp}})^4]$ , with exponential tapering at  $R_{\text{exp}} = 100$  km and a total mass of 0.04 Earth masses. Chondrules have diameters from 0.02 mm to 1.6 mm, in broad agreement with observed chondrule sizes (3). The growth of particles and the formation of chondrule precursors is discussed in the Supplementary Material. We place 0.2 Earth masses of chondrules

initially in the annulus while another 0.2 Earth masses is created continuously over a time span of 3 Myr. The chondrules are given a Gaussian density distribution around the mid-plane, with the scale-height set through a nominal value of the turbulent viscosity of  $\alpha = 10^{-4}$ . The gas in the protoplanetary disk is depleted exponentially on a time-scale of 3 Myr (7).

We show in the left panel of Figure 5 the size distribution after 5 Myr of accreting chondrules. The steep drop in the initial number of planetesimals larger than 100 km in radius has become much shallower because of chondrule accretion, forming a characteristic bump at 60-70 km radius. The size distribution of smaller asteroids in today's belt was likely filled later with fragments from collisional grinding (20). The steep size distribution of larger asteroids ends at around 200 km as even larger asteroids would need to accrete chondrules larger than millimeter in size (see equation 2). At this point the largest asteroids enter a more democratic growth phase where the accretional cross sections are reduced by gas friction within the Bondi radius (23, 24). The agreement with the observed size distribution of asteroids is excellent in the nominal model, except in the range around Ceres mass where it predicts too few objects by a factor of approximately 2-3. Changing the model parameters (using larger chondrules or smaller planetesimal birth sizes) yields poorer agreement with observed asteroid sizes. This implies that the observed size distribution of asteroids is directly determined by the size distribution of the chondrules and the birth sizes of the planetesimals.

The right panel of Figure 5 shows that the major growth phase of asteroids with final radii ranging from 200 km to 500

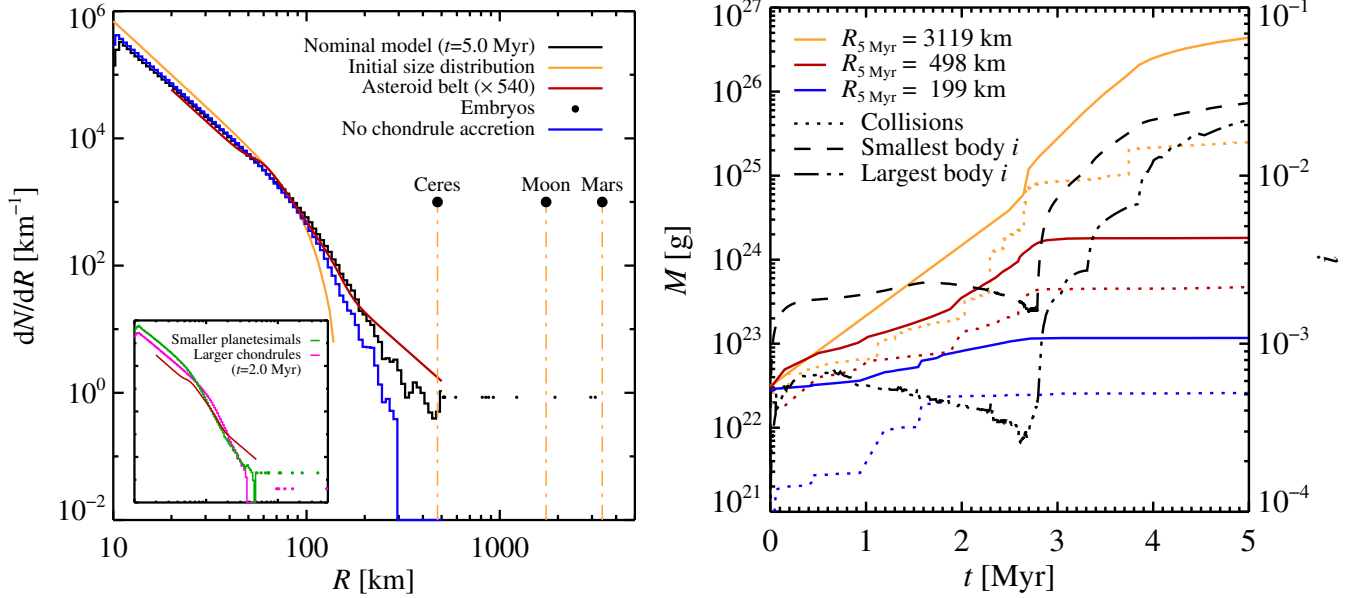


Figure 5: The size distribution of asteroids and embryos after accreting chondrules for 5 Myr (left panel) and selected masses and inclinations as a function of time (right panel). The nominal model (black line) matches closely the steep size distribution of main belt asteroids (red line, representing the current asteroid belt multiplied by a depletion factor of 540) from 60 km to 200 km in radius. The size distribution becomes shallower above 200 km; this is also seen in the asteroid belt, although the simulations underproduce Ceres-sized planetesimals by a factor of approximately 2–3. A simulation with no chondrules (blue line) produces no asteroids larger than 300 km. Inclusion of chondrules up to cm sizes (pink line in insert) gives a much too low production of Ceres-sized asteroids, while setting the exponential cut-off radius of planetesimals to 50 km (green line) leads to a poorer match to the bump at 60 km. The right plot shows that the formation of the first embryos after 2.5 Myr quenches chondrule accretion on the smaller asteroids by exciting their inclinations  $i$  (right axis). The dotted lines indicate the mass contribution from planetesimal-planetesimal collisions. Asteroids and embryos larger than 200 km in radius owe at least 2/3 of their mass to chondrule accretion.

km occurs after 2.5 Myr. Beyond this time the largest planetesimals in the population grow to become planetary embryos with sizes similar to the Moon and Mars. These growing embryos excite the inclinations of the smaller asteroids to  $i \sim 0.01$ , which disconnects the asteroids from the chondrules in the mid-plane layer, quenching their accretion of further chondrules. The beginning of embryo formation terminates the accretion of asteroids after 3 Myr, thus defining the final sizes of the asteroid belt population. The absence of such planetary embryos in today’s asteroid belt may reflect a later depletion by gravitational perturbations from Jupiter (25–27). Depletion of the asteroid belt is discussed further in the Supplementary Text. An important implication of chondrule accretion is that accretion of other planetesimals contributes only a minor fraction to the final masses of large asteroids and embryos (right panel of Figure 5).

### Size sorting of chondrules

Chondrules in chondrites appear strongly size-sorted (8, 28), with the average chondrule diameter varying among the ordinary chondrites (28) from 0.3 mm (H chondrites) up to 0.5 mm (L and LL chondrites). Carbonaceous chondrites exhibit

a larger range in chondrule sizes, from 0.1 to 1 mm. In Figure 6 we show that the mean diameter of accreted chondrules in our model lies in a range similar to that observed for chondrites. The size distribution of accreted chondrules is very narrow, also in agreement with the observed size distribution in the ordinary chondrites (28). The chondrule accretion process, which leads to aerodynamical sorting of chondrules, may thus represent the underlying physical mechanism for the size sorting of chondrules observed in chondrite meteorites. Although aerodynamical sorting has been previously proposed to arise from the gas flow around asteroids (29), our simulations show that accretion from the full Bondi radius is much more efficient in achieving aerodynamical sorting of chondrules.

### Terrestrial planet formation with chondrules

Our identification of chondrule accretion as driving planetesimal growth in the asteroid belt implies that chondrules could play an important role for terrestrial planet formation as well. To test this hypothesis we have performed a numerical integration of the evolution of planetesimal orbits and sizes at 1 AU (Figure 7). The left panel shows the size distribution of the planetesimals at 0, 1, 3 and 5 Myr. Growth to super-Ceres-sized



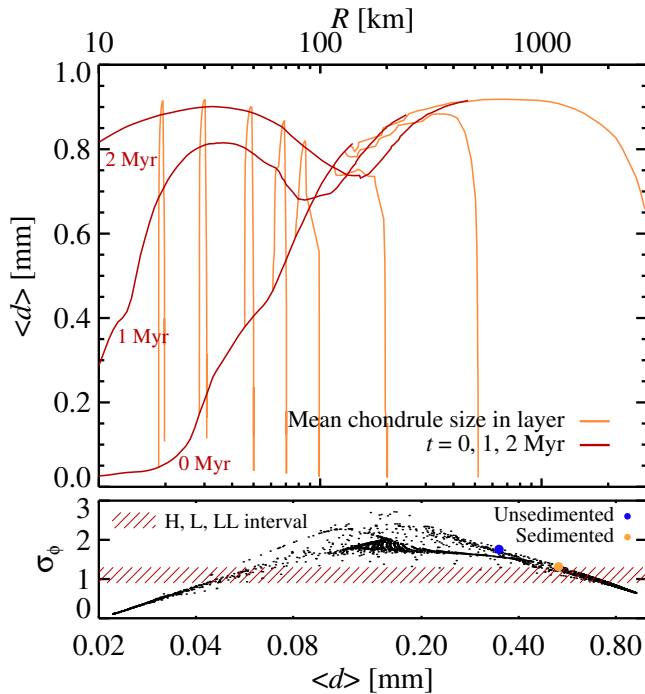


Figure 6: Mean chondrule sizes ( $\langle d \rangle$ , upper panel) as a function of layer radius  $R$  and size-distribution width ( $\sigma_\phi$ , lower panel) as a function of mean chondrule size. Yellow lines in the upper panel indicate the chondrule size evolution in individual asteroids and embryos, while red lines indicate mean accreted chondrule sizes at different times. The accreted chondrule size increases approximately linearly with planetesimal size at  $t = 0$  Myr. Asteroids stirred by the growing embryos over the next 2 Myr accrete increasingly larger chondrules, as asteroid velocities align with the sub-Keplerian chondrule flow at aphelion. Finally, asteroids accrete surface layers of mainly very small chondrules, down to below 0.1 mm in diameter, at late times when their large inclinations decouple the asteroid orbits from the large chondrules in the mid-plane. The width of the chondrule size distribution in the lower panel is given in terms of  $\sigma_\phi$ , the base-2-logarithmic half-width of the cumulative mass distribution of chondrules ( $\sigma_\phi = 1$  implies that 2/3 of the chondrules have diameters within a factor  $2^1 = 2$  from the mean). Dots indicate chondrule layers inside asteroids and embryos. Chondrules are aerodynamically sorted by the accretion process, to values of  $\sigma_\phi$  in agreement with the chondrules found in ordinary chondrites (hashed region). Unfiltered accretion from the background size distribution of chondrules (blue dot: size distribution of un-sedimented particles; yellow dot: size distribution in the mid-plane) yields specific pairs of  $\langle d \rangle$  and  $\sigma_\phi$  that are not consistent with constraints from ordinary chondrites.

planetesimals is rapid and happens within 1 Myr. This growth is driven mainly by planetesimal accretion, in stark contrast to

the situation at 2.5 AU. This is seen in the right panel of Figure 7 where the mass of the largest body is shown as a function of time (full line) together with the mass contribution from chondrules (dashed line) and from planetesimals (dash-dotted line). However, chondrule accretion becomes dominant after 1.5 Myr and drives the further growth up to Mars-mass embryos after 4 Myr. The largest body experiences a giant impact after 4 Myr, after which it continues to grow by chondrule accretion towards 0.9 Earth masses.

Chondrule accretion can thus promote the growth of the largest embryos from Moon masses towards Mars masses and finally Earth masses. The dominance of planetesimal accretion in the initial growth towards Moon masses occurs because chondrules couple tightly to the gas at 1 AU. Here the gas density is more than a factor 10 higher than at 2.5 AU. This prevents sedimentation, such that all chondrule sizes are well mixed with the gas, and it reduces the cross section for accreting chondrules since tightly coupled particles can not be accreted from the full Bondi radius. This situation changes as gas dissipates exponentially over 3 Myr, increasing the friction times and thus the accretion efficiency of the chondrules. Furthermore, the increasingly large embryos obtain high accretion radii for chondrules and hence high chondrule accretion rates, despite the relatively low degree of sedimentation of chondrules present at 1 AU orbits.

Chondrules also play a critical role in terrestrial planet formation in a different way, namely by breaking the isolation mass configuration. Growth by pure planetesimal accretion tends to end in oligarchic growth where the largest embryos are isolated from each other by approximately 10 Hill radii (30). We have implemented the effect of this isolation tendency by identifying the group of isolated bodies as those that can fit their combined reach of 10 Hill radii into the annulus of 0.2 AU in diameter (31, 32). Isolated bodies are not allowed to accrete each other and only affect each other dynamically via distant viscous stirring in the eccentricity. Inclination perturbations, as well as dynamical friction in the eccentricity, are ignored between isolated bodies.

We mark the isolation mass of approximately  $0.01 M_E$  in the right plot of Figure 7 (blue line). A simulation performed with no chondrule accretion (red line) shows the expected growth of the largest embryos to just below the isolation mass. The growth curve for pure planetesimal accretion follows closely the growth curve for the full simulation until approximately  $10^{-4}$  Earth masses. At this point chondrule accretion becomes significant and the two curves diverge. Importantly, chondrule accretion can destabilise a set of isolated bodies, as their continued growth by chondrule accretion drives the least massive of the isolated bodies out of isolation. Hence the giant impacts experienced by the largest embryo between 1.5 and 4 Myr are all driven by chondrule accretion, as these impacts happen beyond the isolation mass.

The importance of chondrule accretion increases if chondrules in the terrestrial planet formation region are larger,

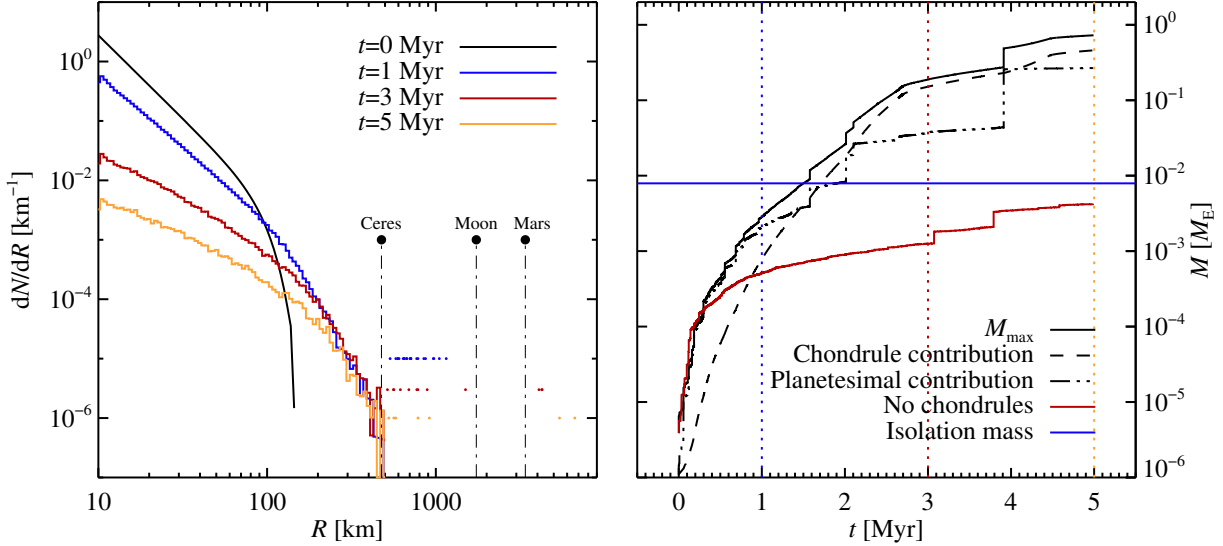


Figure 7: Growth of embryos and terrestrial planets at 1 AU. The left panel shows the size distribution at four different times and the right panel shows the mass of the most massive body in the simulation as a function of time. The growth up to 1000-km-sized embryos is mainly driven by planetesimal accretion, since chondrule-sized pebbles are tightly coupled to the gas and hence hard to accrete. However, chondrule accretion gradually comes to dominate the accretion as the embryos grow. The largest body reaches Mars size after 3 Myr, with more than 90% contribution from chondrule accretion. A giant impact occurs just before 4 Myr, where the largest body accretes the third largest body in the population. The continued accretion of chondrules leads to the formation of an Earth-mass body after 5 Myr. A simulation with no chondrules evolves very differently: a large number of embryos form with masses just below the isolation mass of  $M_{\text{iso}} \approx 0.01 M_{\text{E}}$ .

namely up to 1 cm (macrochondrules). We show the results of expanding the size distribution of chondrules up to 1 cm in Figure 8. Here the initial growth has equal contribution from chondrules and planetesimals. The growth towards embryos and terrestrial planets is much more rapid than in Figure 7; a planet with the mass of the Earth already forms after 1.5 Myr.

The final size of embryos and planets forming by combined planetesimal accretion and chondrule accretion depends on the exact timing of disk dissipation. If the inner disk already dissipates after 3 Myr, then the terrestrial planet formation region will be dominated by a number of Mars-sized embryos. These bodies can go on to partake in a traditional terrestrial planet formation scenario of gradual orbital perturbations and giant impacts over the next 30–100 Myr (33). In contrast, later disk dissipation or the presence of large chondrules in the terrestrial planet formation region allows for the direct formation of planetary bodies within a few Myr. This is far more rapid than traditional terrestrial planet formation scenarios that do not consider chondrule accretion.

### Pebble accretion in the Kuiper belt

The size distribution of trans-Neptunian objects has a characteristic bump around 50 km in radius (34), similar to main belt asteroids, followed by a steep decline towards larger sizes (20). We therefore explore here whether accretion of chondrules and icy pebbles could be responsible for the observed size distribu-

tion of Kuiper belt objects as well.

The asteroid belt displays a value of  $q \approx 4.5$  in the size distribution  $dN/dR \propto R^{-q}$  of asteroids larger than 60 km in radius, while the hot population of the classical Kuiper belt and the Neptune trojans have a much higher value of  $q \approx 5 \dots 6$  for large planetesimals (35). The cold population of the classical Kuiper belt has an even steeper decline, with  $q \approx 8 \dots 9$ . The planetesimals in the cold population are believed to have formed in situ in the outermost regions of the solar system (36), while the hot population and scattered disk objects formed outside the birth location of Neptune and were subsequently pushed outwards by Neptune’s migration to its current orbit (37, 38). The planetesimals which formed between the orbits of Jupiter and Neptune may today be represented by the C-type asteroids, scattered to the asteroid belt during Jupiter’s migration (27). In order to probe planetesimal growth by chondrule accretion (or icy particles of a similar size range) beyond the asteroid belt, we therefore consider the two characteristic distances 10 AU and 25 AU.

### Planetesimal growth at 10 AU

The region around 10 AU represents the conditions where the gas giants formed. The formation of Jupiter and Saturn must have had an enormous effect on the planetesimals in that region, with some ejected to the Oort cloud and others potentially mixed into the outer asteroid belt during Jupiter’s and

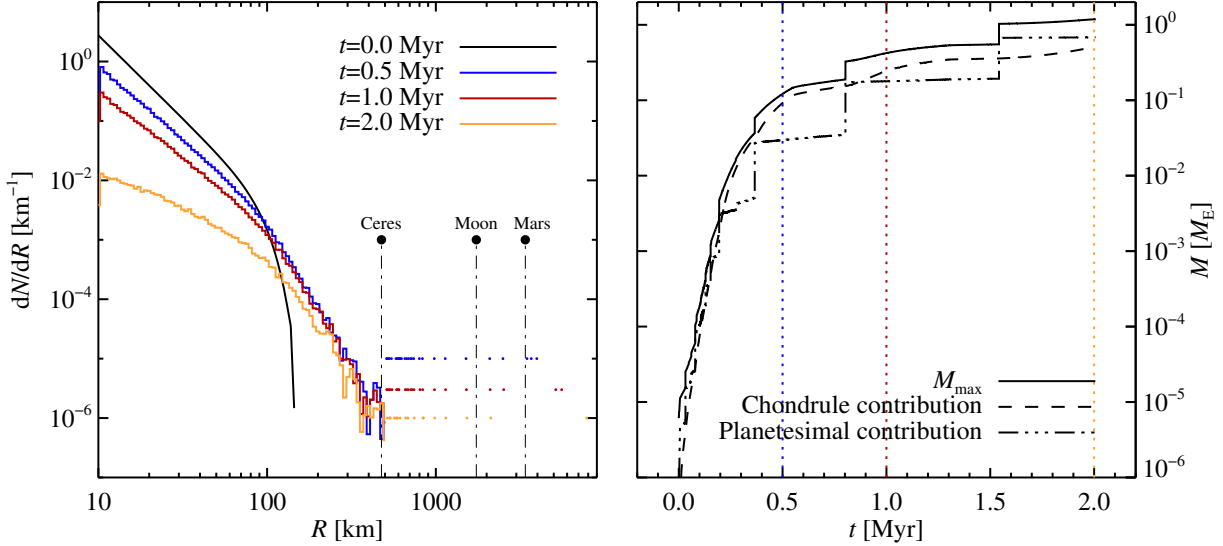


Figure 8: Growth of embryos and terrestrial planets at 1 AU, with chondrule sizes up to 1 cm. The increase in chondrule size compared to the previous figure enhances the chondrule accretion rate substantially. The initial growth to 1000-km-sized embryos now has approximately equal contribution from planetesimal accretion and chondrule accretion. An Earth-mass terrestrial planet forms already after 2 Myr, driven by a combination of chondrule accretion and giant impacts.

Saturn’s migration (27). To test how the size distribution of planetesimals evolves at 10 AU, we set up an annulus of width 0.2 AU. The planetesimals are again given sizes from 10 to 150 km in radius, with a steep exponential tapering above 100 km. The internal density of the planetesimals is set to  $2 \text{ g/cm}^3$ , similar to that of Ceres, a typical representative of the icy asteroids in the outer part of the main belt. The pebbles have radii from 0.01 to 1 mm. These pebbles could represent a mixture of chondrules transported outwards from the inner solar system and icy pebbles formed beyond of the ice line. Chondrules may also have formed in situ in the outer parts of the protoplanetary disk. In fact, some chondrules present in carbonaceous chondrites have  $^{50}\text{Ti}/^{47}\text{Ti}$  ratios comparable to those of the most pristine chondrites, namely the CI carbonaceous chondrites (6). This suggests that at least a fraction of chondrules in carbonaceous chondrites formed from pristine, thermally unprocessed precursor material typical of the accretion regions of CI chondrites. Given that these chondrites are believed to have accreted beyond the ice line (27), chondrule formation appears to not have been limited to the asteroidal belt, but also occurred in the outer solar system.

The results at 10 AU are shown in Figure 9. Planetesimals of Ceres size grow within approximately 2 Myr, followed by the usual phase of embryo growth also seen in Figure 5. The largest embryo reaches a mass comparable to the Earth’s before 3 Myr. The mid-plane density of pebbles is much lower at 10 AU than at 2.5 AU, but this is more than counter-acted by increased sedimentation of particles in the dilute gas. The size distribution is very steep, much steeper than in the asteroid belt,

and resembles better the steepness of the size distribution of the trans-Neptunian populations (35). Finally, it is interesting to note that at these orbital distances planetesimal-planetesimal collisions are even less important than at 2.5 AU (right panel of Figure 9). The Earth-mass protoplanet has only a few parts in a thousand contribution from planetesimal collisions.

#### Planetesimal growth at 25 AU

In the outer regions of the protoplanetary disk we adopt a model where the surface density profile is proportional to the inverse of the orbital radius. This is in agreement with surface density profiles of observed protoplanetary disks (39, 40). Hence we set the total column density of particles at  $r = 25 \text{ AU}$  to  $\Sigma_p = 0.54 \text{ g/cm}^2$ . We set the temperature at 25 AU according to full radiative transfer models of protoplanetary disks. This is important, since the optically thin assumption in the Minimum Mass Solar Nebula model of Hayashi (19) overestimates the temperature in the outer disk. The growth rate of a planetesimal with mass  $M_p$  by pebble accretion is given by

$$\dot{M}_p = \pi f_B^2 \left[ \frac{GM_p}{(\Delta v)^2} \right]^2 (\Delta v) \rho_p. \quad (3)$$

Here  $f_B$  denotes the ratio of the actual accretion radius to the Bondi radius (24),  $\Delta v$  is the sub-Keplerian speed difference and  $\rho_p$  is the mid-plane particle density. The sub-Keplerian speed is given by

$$\Delta v = -\frac{1}{2} \frac{H}{r} \frac{\partial \ln P}{\partial \ln r} c_s. \quad (4)$$

The speed difference scales with the sound speed as  $c_s^2$ , since  $H/r$  contains another  $c_s$ . Hence the accretion rate scales with



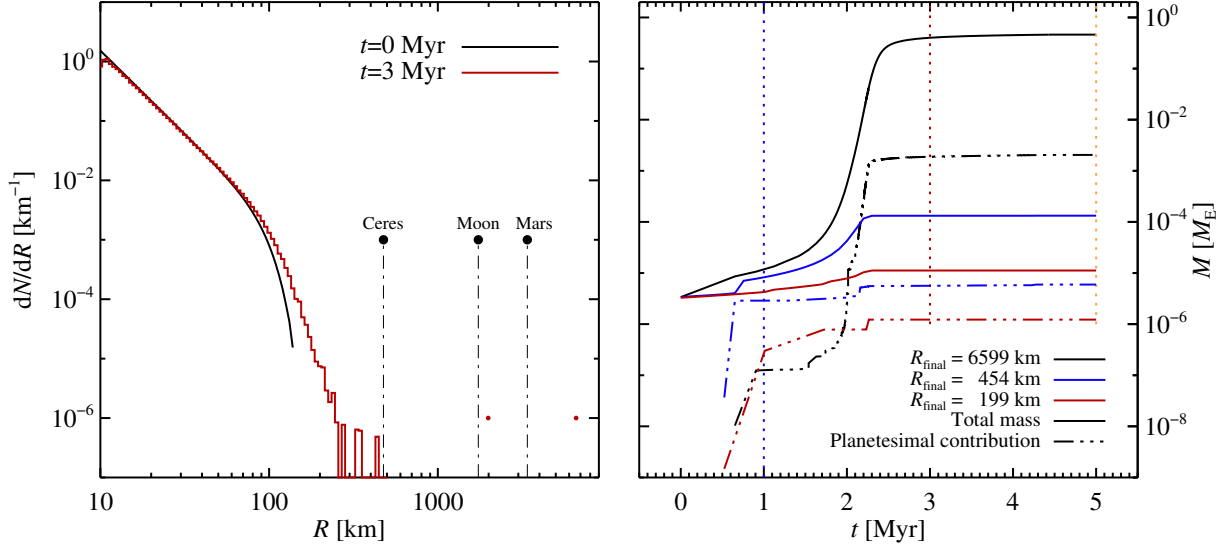


Figure 9: Growth of icy planetesimals at 10 AU. The growth rate by pebble accretion is as high as in the asteroid belt, since the lower column density of pebbles is counter-acted by the increased sedimentation in the more dilute gas. The annulus of 0.2 AU width produces in the end an Earth-sized protoplanet and a single Moon-sized embryo. Pebble accretion overwhelmingly dominates the growth (right panel). The icy protoplanet that forms has only a few parts in a thousand mass contribution from collisions. Large Ceres-sized planetesimals have a contribution from collisions of less than 5%, while the 200 km planetesimal owes about 1/10 of its growth from 130 km to planetesimal collisions. Note how the Ceres-sized planetesimal (blue line in the right panel) got a head start for efficient accretion of pebbles by experiencing a significant collision after 700,000 years.

the sound speed to the negative sixth power, and the sound speed must be set carefully to yield realistic results. We set the sound speed at 25 AU through the aspect ratio  $H/r = 0.05$ , based on radiative transfer models of protoplanetary accretion disks (41). This is much smaller than the standard value in the Minimum Mass Solar Nebula ( $H/r = 0.072$  at  $r = 25$  AU) and leads to much higher accretion rates in the outer nebula.

We consider two models for planetesimal growth at 25 AU. First, a low density model where the internal density of the planetesimals is set to  $0.5 \text{ g/cm}^3$ , similar to comets and some binary Kuiper belt objects (42). Second, a high density model that has instead an internal density of  $2 \text{ g/cm}^3$ , more in agreement with the icy dwarf planets Pluto and Ceres. The low density model experiences much lower pebble accretion rates because of the reduced gravity of the planetesimals. We find that a turbulent stirring of  $\alpha = 10^{-4}$ , which we used for the asteroid belt, results in growth times for pebble accretion of more than 10 Myr. Hence we set the turbulent stirring to a low value of  $\alpha = 10^{-6}$  in the low density model. The high density model has  $\alpha = 10^{-5}$ . We discuss in the next section how such low values could arise physically.

We show the resulting size distributions and growth curve of the largest body at 25 AU in Figure 10. The size distributions in the left panel of the figure both display a steep power law beyond 100 km in radius. Planetesimals up to 300 km in radius accrete significant amounts of pebbles. Beyond 300 km a

run-away growth sets in where the largest body detaches from the remaining population (right panel of Figure 10). This run-away growth is possible because of the weak gas friction at 25 AU. Hence run-away pebble accretion is not slowed down by reaching the strong coupling branch but can instead continue to very large sizes (see Supplementary Material and Figures S7 and S6).

Altogether it is clear that pebble accretion at 25 AU is much slower than at 2.5 AU, and actually requires very low turbulent activity for significant growth. But planetesimal growth in such wide orbits apparently also has the potential to result in run-away accretion up to ice giant sizes. The size distribution of planetesimals from 100 to 300 km in radius is very steep, in good qualitative agreement with what is observed in the present Kuiper belt (35). Our results show that 25 AU can be considered the very limit to where pebble accretion is significant, and then only for weak turbulence. Beyond this radius planetesimals maintain their birth sizes (and size distribution), and hence the very steep size distribution of large planetesimals in the cold component of the classical Kuiper belt may reflect the actual exponential cut off in the underlying birth size distribution.

In the solar system, Neptune stopped its outwards migration at 30 AU. Therefore the primordial Kuiper belt can not have extended much beyond that distance, as otherwise Neptune would have continued to migrate outwards by scattering planetesi-

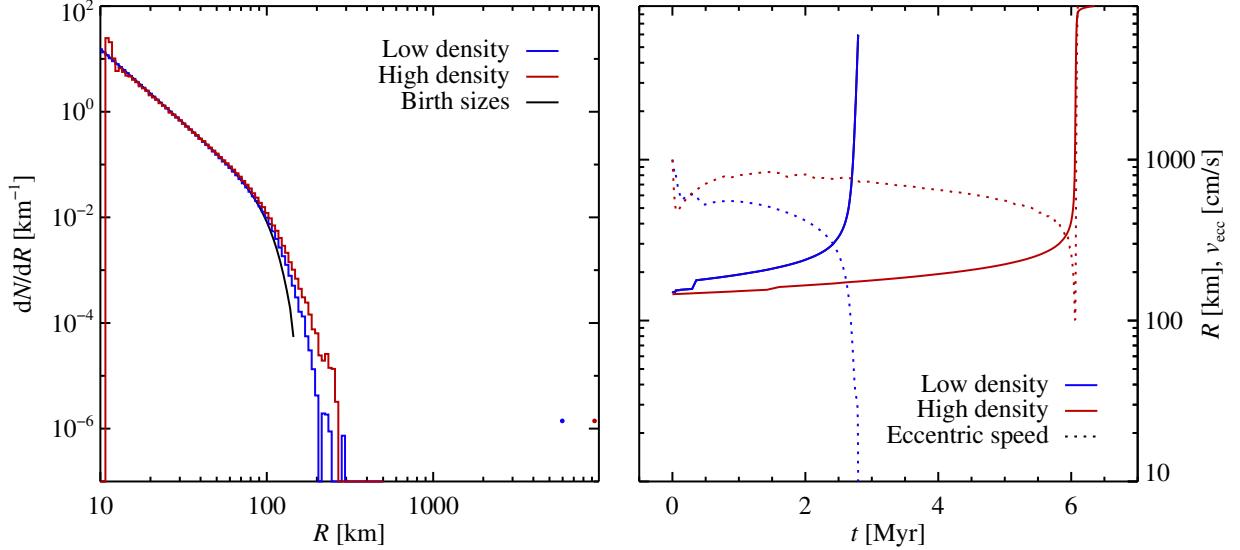


Figure 10: Planetesimal growth at 25 AU. Two models are considered, a *low density model* where the internal density is set to  $\rho_{\bullet} = 0.5 \text{ g/cm}^3$ , similar to comets and binary Kuiper belt objects, and a *high density model* where the internal density is set to  $\rho_{\bullet} = 2 \text{ g/cm}^3$ , similar to the dwarf planet Ceres. The low density model has turbulent stirring  $\alpha = 10^{-6}$  while the high density model has  $\alpha = 10^{-5}$ . Both models display ordered growth up to 300 km radii, with a steep size distribution beyond 100 km sizes. This is followed by a run-away growth of a single, massive body. The right panel shows the size of the largest body as a function of time as well as the speed relative to a circular orbit. The run-away growth is facilitated by a steep decline in the eccentricity of the orbit, as the high pebble accretion rate damps the eccentricity.

mals (38). However, the presence of the cold population, which appears detached from Neptune, indicates that the Kuiper belt could simply have transitioned to a much lower surface density around 30 AU. The planetesimals there did not grow beyond their birth sizes, resulting in a jump in the planetesimal column density between the regions inside 25 AU which experienced growth by pebble accretion and the regions outside which did not.

## Discussion

### Variation of turbulence strength

An important and relatively unconstrained parameter in our chondrule accretion model for the formation of asteroids and planetary embryos is the strength of the turbulence in the protoplanetary disk, as the turbulent diffusion coefficient sets the scale-height of the particle layer and the mid-plane density of the chondrules ( $I$ ). The asteroid formation region is located in a region of the protoplanetary disk where the degree of ionisation is believed to be too low to sustain turbulence driven by the magnetorotational instability. The ionisation degree in the surface layers may nevertheless be high enough to drive accretion there. The turbulent motion in these layers will stir the otherwise laminar mid-plane. Effective turbulent viscosities between  $\alpha = 10^{-5}$  and  $\alpha = 10^{-4}$  have been measured in the mid-plane in computer simulations of dead zone stirring (43).

Models of protoplanetary accretion disks that also include

the effect of ambipolar diffusion in the surface layers find that the growth of the magnetorotational instability is quenched even there, by the lack of coupling between electrons and neutrals (44). The magnetic field may enter a configuration where gas (and angular momentum) is expelled upwards, while gas connected to the magnetic field lines closer to the mid-plane is accreted towards the star. This disk wind accretion leaves the mid-plane completely laminar. The sedimentation of dust will nevertheless cause a mild stirring of the mid-plane (45). The stirring caused by streaming and Kelvin-Helmholtz instabilities in the dense mid-plane layer of chondrules will be much milder than the stirring from the active layers, with a typical value of  $\alpha = 10^{-6}$  for chondrule-sized particles.

The nominal value for the turbulent diffusion coefficient in our model is  $\alpha = 10^{-4}$ , corresponding to conditions in a dead zone stirred by active surface layers. To quantify the effect of the turbulent stirring of chondrules on our results we have run simulations with a lower ( $\alpha = 2 \times 10^{-6}$ ) and a higher ( $\alpha = 10^{-3}$ ) value of the turbulent diffusion coefficient. The size of the largest planetesimal in the asteroid belt is shown as a function of time in Figure 11. Clearly, a lower value of the turbulent diffusion coefficient results in a much higher growth rate of the planetesimals, as chondrules are allowed to sediment much more strongly to the mid-plane. For  $\alpha = 10^{-3}$  the formation of the first embryos is delayed to after 5 Myr, which is longer than the typical life-times of protoplanetary disks around

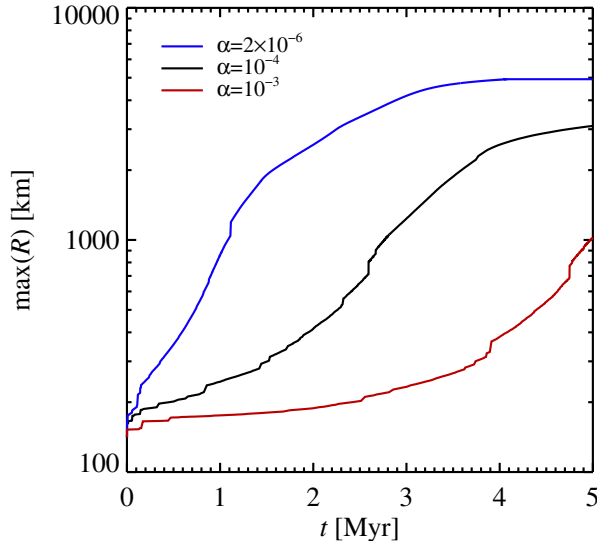


Figure 11: The maximum planetesimal radius in the asteroid belt versus time, for three different values of the turbulent viscosity  $\alpha$ . Here  $\alpha = 2 \times 10^{-6}$  represents the strength of turbulence caused by streaming instabilities and Kelvin-Helmholtz instabilities in a sedimented mid-plane layer of chondrules,  $\alpha = 10^{-4}$  represents the turbulence strength in a dead zone stirred by active surface layers and  $\alpha = 10^{-3}$  the turbulence strength caused directly by the magnetorotational instability. Turbulent stirring of chondrules sets the scale-height and mid-plane density of the chondrule layer and hence dictates the planetesimal growth rate. The formation time of the first embryo depends strongly on the degree of stirring.

young stars.

### Layered accretion in the asteroid belt

Our model provides a direct connection between chondrules and asteroid growth. While early accreted asteroids and their chondrules would melt from the energy released by the decay of the short-lived  $^{26}\text{Al}$  radionuclide, layers accreted later than 2 Myr may preserve their pristine, undifferentiated nature (46). Indeed, the existence of differentiated asteroids overlaid by chondritic crusts has been proposed to explain the systematic magnetisations of chondrules in the Allende meteorite (47, 48), imprinted from a geodynamo operating in the liquid central region of the parent body. The asteroid Lutetia has been suggested to be partially differentiated, due to its high mean density and primitive surface (49).

The characteristic maximum size of planetesimals formed through streaming instabilities is 50–150 km in radius for column densities comparable to the Minimum Mass Solar Nebula (Figure 3). Planetesimals much smaller than 100 km in radius are relatively inefficient at accreting chondrules and hence accrete only a thin veneer of chondrules on top of the primordially formed planetesimal (Figure 5 and Figure 6). Planetesi-

imals forming before 1–2 Myr after CAIs will likely differentiate, as was the case for the parent bodies of the differentiated meteorites (50, 51). Hence we predict that asteroids currently residing in the knee at the size distribution at 60 km radii represent primordial, differentiated bodies overlain by a veneer of chondrules of thickness up to a few dozen kilometers.

Asteroids larger than 100 km in radius, on the other hand, grow mainly by accretion of chondrules. The initial planetesimal seeds will be covered with extended layers of narrowly size-sorted chondrules. The Allende meteorite, whose systematic magnetisation makes the parent body a prime candidate for layered accretion, has been proposed to originate from the Eos family in the asteroid belt (52). This family is known to display significant spectral variations between its members (52), indicating partial differentiation and internal heterogeneity of the 110-km-radius parent body. Another example of an asteroid family with large internal variation in the spectral properties is the Eunomia family (48), believed to originate from a parent body of 150 km in radius. Intermediate-sized asteroids of 100–200 km in radius appear to be the best candidates for producing such families with large internal variation. Bodies of this size range have comparable mass fractions in the differentiated planetesimal seed and in the accreted chondrule layers.

Many other asteroid families display internal albedo distributions that are much narrower than the spread of albedos across families (53), in stark contrast to the heterogeneous Eos and Eunomia families discussed above. The inference of the internal structure of the parent bodies of such apparently homogeneous families is nevertheless complicated by the identification of interlopers in (and exclusion from) the asteroid families. A family member whose albedo is different from the family mean could in fact be mistaken for an interloper. However, the identification of asteroid families that appear to originate from internally homogeneous asteroids is not in conflict with our model. Our results show that many asteroids in the 50–100 km radius range will have experienced little chondrule accretion and represent primordial asteroid seeds. Additionally, very large asteroids of radii larger than 300–400 km must have undergone significant accretion of chondrules between 2 and 3 Myr after the formation of the seed planetesimal. Families formed mainly from the chondrule layers of such large asteroids would also appear relatively homogeneous. Fragments as large as 100 km in radius could consist of purely chondritic material, and families produced from those fragments would in turn appear entirely homogeneous.

### Implications for terrestrial planet formation

The largest planetesimals in our simulations of the asteroid belt and the terrestrial planet formation region grow to sizes of several thousand kilometers, forming the embryos whose mutual collisions drive the subsequent terrestrial planet formation stage. With only 11% of Earth’s mass, Mars may be one of these remaining embryos. Mars is inferred to have accreted  $2 \pm 1$  Myr after the first condensations in the solar system (54), in good agreement with the formation time-scale of planetary

embryos by chondrule accretion in our simulations. This implies that chondrule accretion is a driving mechanism ensuring the rapid growth of planetary embryos in the terrestrial planet formation region. Thus the production of chondrules may be a key process promoting the assembly of rocky planets.

## Materials and Methods

### Planetesimal formation simulations

The planetesimal formation simulations were performed with the Pencil Code (which can be freely downloaded, including modifications done for this work, at <http://code.google.com/pencil-code>). A new sink particle algorithm developed for this project is presented in the Supplementary Material.

Our simulations of planetesimal formation through streaming instabilities are performed in the local shearing box frame. The simulation box orbits with the local Keplerian frequency  $\Omega$  at an arbitrary radial distance  $r$  from the central star. We fix the box size to a cube of side lengths  $L = 0.2H$ , where  $H$  is the gas scale-height. The box size is chosen in order to capture the relevant wavelengths of the streaming instability (55). The gas is initialised with a Gaussian density profile around the mid-plane, in reaction to the component of stellar gravity directed towards the mid-plane. The temperature is assumed to be a constant set through the sound speed  $c_s$ , which is kept fixed during the simulation. Particles are given positions according to a Gaussian density distribution, with a scale-height of 1% of the gas scale-height. We assume that particles in the entire column have sedimented into the simulation domain, giving a mean solids-to-gas ratio of  $\langle \rho_p \rangle / \rho_0 \approx 0.25$  for the chosen metallicity  $Z = 0.01$ . The particles have uniform sizes given by the Stokes number  $St = \Omega t_f = 0.3$ , where  $t_f$  is the friction time of the particles, corresponding to approximately 25-cm-sized particles at 2.5 AU. It has previously been shown that the consideration of a range of particles sizes gives similar results to the monodisperse case (12).

The strength of the particle self-gravity in a scale-free local box simulation is set by the non-dimensional parameter

$$\Gamma = \frac{4\pi G \rho_0}{\Omega^2} \approx 0.036 \left( \frac{r}{2.5 \text{ AU}} \right)^{1/4}. \quad (5)$$

Here  $G$  is the gravity constant,  $\rho_0$  is the gas density in the mid-plane and  $\Omega$  is the Keplerian frequency at the chosen radial distance from the star. The scaling with semi-major axis is based on the properties of the Minimum Mass Solar Nebula (19). The parameter  $\Gamma$  multiplied by the non-dimensional particle density  $\rho_p / \rho_0$  enters the Poisson equation for self-gravity,  $\nabla^2 \Phi = 4\pi G \rho_p$ , when lengths are measured in units of the scale-height and times in units of the inverse Keplerian frequency  $\Omega^{-1}$ . The parameter also converts a given mass density of particles in a grid cell to an actual mass, since the choice of  $\Gamma$  defines the mid-plane gas density  $\rho_0$ . Thus both the dynamics and resulting planetesimal masses are strongly influenced by the value of  $\Gamma$  (this is also evident from the results presented in Figure 3).

### Chondrule accretion simulations

We have developed a statistical code which evolves the masses and orbits of planetesimals as they accrete chondrules and collide mutually. Details of the code algorithms, test calculations as well as comparisons to other published results are presented in the Supplementary Materials and Methods.

## Acknowledgments

### General

We are grateful to Glen Stewart, Alessandro Morbidelli, Jeff Cuzzi and Michiel Lambrechts for stimulating discussions. We would like to thank the anonymous referees for many helpful suggestions which helped to improve the paper.

### Funding

A.J. is grateful for the financial support from the European Research Council (ERC Starting Grant 278675-PEBBLE2PLANET), the Knut and Alice Wallenberg Foundation and the Swedish Research Council (grant 2010-3710). M.-M.M.L. was partly supported by NASA Origins of Solar Systems grant #NNX14AJ56G, NSF grant AST10-09802, and the Alexander von Humboldt-Stiftung. M.B. acknowledges funding from the Danish National Research Foundation (grant number DNRF97) and by the European Research Council (ERC Consolidator Grant 616027-STAR DUST 2 ASTEROIDS). This work was granted access to the HPC resources of Research Centre Jülich, Irish Centre for High-End Computing and Rechenzentrum Garching, made available within the Distributed European Computing Initiative by the PRACE-2IP (PRACE project “PLANETESIM”), receiving funding from the European Community’s Seventh Framework Programme (FP7/2007-2013) under grant agreement no. RI-283493.

## References

1. A. Johansen, *et al.*, The multifaceted planetesimal formation process. *Protostars and Planets VI* (2014).
2. S. N. Raymond, E. Kokubo, A. Morbidelli, R. Morishima, K. J. Walsh, Terrestrial Planet Formation at Home and Abroad. *Protostars and Planets VI* (2014).
3. A. N. Krot, K. Keil, C. A. Goodrich, E. R. D. Scott, M. K. Weisberg, Classification of Meteorites. *Treatise on Geochemistry* **1**, 83-128 (2003).
4. K. Metzler, A. Bischoff, D. Stoeffler, Accretionary dust mantles in CM chondrites - Evidence for solar nebula processes. *Geochimica et Cosmochimica Acta* **56**, 2873-2897 (1992).
5. J. N. Connelly, *et al.*, The Absolute Chronology and Thermal Processing of Solids in the Solar Protoplanetary Disk. *Science* **338**, 651- (2012).

6. A. Trinquier, *et al.*, Origin of Nucleosynthetic Isotope Heterogeneity in the Solar Protoplanetary Disk. *Science* **324**, 374- (2009).
7. K. E. Haisch, Jr., E. A. Lada, C. J. Lada, Disk Frequencies and Lifetimes in Young Clusters. *The Astrophysical Journal* **553**, L153-L156 (2001).
8. J. N. Cuzzi, R. C. Hogan, J. M. Paque, A. R. Dobrovolskis, Size-selective Concentration of Chondrules and Other Small Particles in Protoplanetary Nebula Turbulence. *The Astrophysical Journal* **546**, 496-508 (2001).
9. J. N. Cuzzi, R. C. Hogan, K. Shariff, Toward Planetesimals: Dense Chondrule Clumps in the Protoplanetary Nebula. *The Astrophysical Journal* **687**, 1432-1447 (2008).
10. L. Pan, P. Padoan, J. Scalo, A. G. Kritsuk, M. L. Norman, Turbulent Clustering of Protoplanetary Dust and Planetesimal Formation. *The Astrophysical Journal* **740**, 6 (2011).
11. A. N. Youdin, J. Goodman, Streaming Instabilities in Protoplanetary Disks. *The Astrophysical Journal* **620**, 459-469 (2005).
12. A. Johansen, *et al.*, Rapid planetesimal formation in turbulent circumstellar disks. *Nature* **448**, 1022-1025 (2007).
13. A. Johansen, A. Youdin, M.-M. Mac Low, Particle Clumping and Planetesimal Formation Depend Strongly on Metallicity. *The Astrophysical Journal* **704**, L75-L79 (2009).
14. A. Johansen, A. N. Youdin, Y. Lithwick, Adding particle collisions to the formation of asteroids and Kuiper belt objects via streaming instabilities. *Astronomy & Astrophysics* **537**, A125 (2012).
15. X.-N. Bai, J. M. Stone, Dynamics of Solids in the Midplane of Protoplanetary Disks: Implications for Planetesimal Formation. *The Astrophysical Journal* **722**, 1437-1459 (2010).
16. M. Weyrauch, A. Bischoff, Macrochondrules in chondrites – Formation by melting of mega-sized dust aggregates and/or by rapid collisions at high temperatures? *Meteoritics and Planetary Science* **47**, 2237-2250 (2012).
17. C. W. Ormel, J. N. Cuzzi, A. G. G. M. Tielens, Co-Accretion of Chondrules and Dust in the Solar Nebula. *The Astrophysical Journal* **679**, 1588-1610 (2008).
18. F. H. Shu, H. Shang, T. Lee, Toward an Astrophysical Theory of Chondrites. *Science* **271**, 1545-1552 (1996).
19. C. Hayashi, Structure of the Solar Nebula, Growth and Decay of Magnetic Fields and Effects of Magnetic and Turbulent Viscosities on the Nebula. *Progress of Theoretical Physics Supplement* **70**, 35-53 (1981).
20. W. F. Bottke, *et al.*, The fossilized size distribution of the main asteroid belt. *Icarus* **175**, 111-140 (2005).
21. A. Morbidelli, W. F. Bottke, D. Nesvorný, H. F. Levison, Asteroids were born big. *Icarus* **204**, 558-573 (2009).
22. J. N. Cuzzi, R. C. Hogan, W. F. Bottke, Towards initial mass functions for asteroids and Kuiper Belt Objects. *Icarus* **208**, 518-538 (2010).
23. C. W. Ormel, H. H. Klahr, The effect of gas drag on the growth of protoplanets. Analytical expressions for the accretion of small bodies in laminar disks. *Astronomy & Astrophysics* **520**, A43 (2010).
24. M. Lambrechts, A. Johansen, Rapid growth of gas-giant cores by pebble accretion. *Astronomy & Astrophysics* **544**, A32 (2012).
25. G. W. Wetherill, An alternative model for the formation of the asteroids. *Icarus* **100**, 307-325 (1992).
26. D. A. Minton, R. Malhotra, A record of planet migration in the main asteroid belt. *Nature* **457**, 1109-1111 (2009).
27. K. J. Walsh, A. Morbidelli, S. N. Raymond, D. P. O'Brien, A. M. Mandell, A low mass for Mars from Jupiter's early gas-driven migration. *Nature* **475**, 206-209 (2011).
28. R. T. Dodd, Accretion of the ordinary chondrites. *Earth and Planetary Science Letters* **30**, 281-291 (1976).
29. F. L. Whipple, Accumulation of Chondrules on Asteroids. *NASA Special Publication* **267**, 251 (1971).
30. E. Kokubo, S. Ida, Oligarchic Growth of Protoplanets. *Icarus* **131**, 171-178 (1998).
31. S. Inaba, H. Tanaka, K. Nakazawa, G. W. Wetherill, E. Kokubo, High-Accuracy Statistical Simulation of Planetary Accretion: II. Comparison with N-Body Simulation. *Icarus* **149**, 235-250 (2001).
32. K. Ohtsuki, G. R. Stewart, S. Ida, Evolution of Planetesimal Velocities Based on Three-Body Orbital Integrations and Growth of Protoplanets. *Icarus* **155**, 436-453 (2002).
33. D. P. O'Brien, A. Morbidelli, H. F. Levison, Terrestrial planet formation with strong dynamical friction. *Icarus* **184**, 39-58 (2006).
34. S. S. Sheppard, C. A. Trujillo, The Size Distribution of the Neptune Trojans and the Missing Intermediate-sized Planetesimals. *The Astrophysical Journal* **723**, L233-L237 (2010).
35. W. C. Fraser, M. E. Brown, A. Morbidelli, A. Parker, K. Batygin, The Absolute Magnitude Distribution of Kuiper Belt Objects. *The Astrophysical Journal* **782**, 100 (2014).



36. K. Batygin, M. E. Brown, W. C. Fraser, Retention of a Primordial Cold Classical Kuiper Belt in an Instability-Driven Model of Solar System Formation. *The Astrophysical Journal* **738**, 13 (2011).
37. R. Malhotra, The Origin of Pluto's Orbit: Implications for the Solar System Beyond Neptune. *The Astronomical Journal* **110**, 420 (1995).
38. K. Tsiganis, R. Gomes, A. Morbidelli, H. F. Levison, Origin of the orbital architecture of the giant planets of the Solar System. *Nature* **435**, 459-461 (2005).
39. J. P. Williams, L. A. Cieza, Protoplanetary Disks and Their Evolution. *Annual Review of Astronomy & Astrophysics* **49**, 67-117 (2011).
40. T. Birnstiel, H. Klahr, B. Ercolano, A simple model for the evolution of the dust population in protoplanetary disks. *Astronomy & Astrophysics* **539**, A148 (2012).
41. B. Bitsch, A. Johansen, L. Lambrechts, A. Morbidelli, The structure of protoplanetary discs around evolving young stars. *Submitted to Astronomy & Astrophysics* (2015).
42. M. E. Brown, The Density of Mid-sized Kuiper Belt Object 2002 UX25 and the Formation of the Dwarf Planets. *The Astrophysical Journal* **778**, L34 (2013).
43. J. S. Oishi, M.-M. Mac Low, K. Menou, Turbulent Torques on Protoplanets in a Dead Zone. *The Astrophysical Journal* **670**, 805-819 (2007).
44. X.-N. Bai, J. M. Stone, Wind-driven Accretion in Protoplanetary Disks. I. Suppression of the Magnetorotational Instability and Launching of the Magnetocentrifugal Wind. *The Astrophysical Journal* **769**, 76 (2013).
45. D. Carrera, A. Johansen, M. B. Davies, Formation of asteroids from mm-sized chondrules. *Astronomy & Astrophysics*, submitted, *arXiv:1501.05314* (2014).
46. P. J. Hevey, I. S. Sanders, A model for planetesimal meltdown by  $^{26}\text{Al}$  and its implications for meteorite parent bodies. *Meteoritics and Planetary Science* **41**, 95-106 (2006).
47. L. T. Elkins-Tanton, B. P. Weiss, M. T. Zuber, Chondrites as samples of differentiated planetesimals. *Earth and Planetary Science Letters* **305**, 1-10 (2011).
48. B. P. Weiss, L. T. Elkins-Tanton, Differentiated Planetesimals and the Parent Bodies of Chondrites. *Annual Review of Earth and Planetary Sciences* **41**, 529-560 (2013).
49. M. Pätzold, *et al.*, Asteroid 21 Lutetia: Low Mass, High Density. *Science* **334**, 491- (2011).
50. J. Baker, M. Bizzarro, N. Wittig, J. Connelly, H. Haack, Early planetesimal melting from an age of 4.5662Gyr for differentiated meteorites. *Nature* **436**, 1127-1131 (2005).
51. T. Kleine, *et al.*, Hf-W chronology of the accretion and early evolution of asteroids and terrestrial planets. *Geochimica et Cosmochimica Acta* **73**, 5150-5188 (2009).
52. T. Mothé-Diniz, J. M. Carvano, S. J. Bus, R. Duffard, T. H. Burbine, Mineralogical analysis of the Eos family from near-infrared spectra. *Icarus* **195**, 277-294 (2008).
53. T. Mothé-Diniz, F. Roig, J. M. Carvano, Reanalysis of asteroid families structure through visible spectroscopy. *Icarus* **174**, 54-80 (2005).
54. N. Dauphas, A. Pourmand, Hf-W-Th evidence for rapid growth of Mars and its status as a planetary embryo. *Nature* **473**, 489-492 (2011).
55. C.-C. Yang, A. Johansen, On the Feeding Zone of Planetesimal Formation by the Streaming Instability. *The Astrophysical Journal* **792**, 86 (2014).
56. A. Johansen, H. Klahr, T. Henning, High-resolution simulations of planetesimal formation in turbulent protoplanetary discs. *Astronomy & Astrophysics* **529**, A62 (2011).
57. S. J. Weidenschilling, Initial sizes of planetesimals and accretion of the asteroids. *Icarus* **214**, 671-684 (2011).
58. A. Johansen, P. Lacerda, Prograde rotation of protoplanets by accretion of pebbles in a gaseous environment. *Monthly Notices of the Royal Astronomical Society* **404**, 475-485 (2010).
59. G. K. Batchelor, *An Introduction to Fluid Dynamics* (2000).
60. G. R. Stewart, S. Ida, Velocity Evolution of Planetesimals: Unified Analytical Formulas and Comparisons with N-Body Simulations. *Icarus* **143**, 28-44 (2000).
61. G. W. Wetherill, G. R. Stewart, Accumulation of a swarm of small planetesimals. *Icarus* **77**, 330-357 (1989).
62. G. W. Wetherill, Comparison of analytical and physical modeling of planetesimal accumulation. *Icarus* **88**, 336-354 (1990).
63. S. J. Weidenschilling, Aerodynamics of solid bodies in the solar nebula. *Monthly Notices of the Royal Astronomical Society* **180**, 57-70 (1977).
64. K. Ros, A. Johansen, Ice condensation as a planet formation mechanism. *Astronomy & Astrophysics* **552**, A137 (2013).

65. R. Hutchison, C. M. O. Alexander, D. J. Barber, The Se-markona meteorite - First recorded occurrence of smectite in an ordinary chondrite, and its implications. *Geochimica et Cosmochimica Acta* **51**, 1875-1882 (1987).
66. C. Güttler, J. Blum, A. Zsom, C. W. Ormel, C. P. Dullemond, The outcome of protoplanetary dust growth: pebbles, boulders, or planetesimals?. I. Mapping the zoo of laboratory collision experiments. *Astronomy & Astrophysics* **513**, A56 (2010).
67. A. Zsom, C. W. Ormel, C. Güttler, J. Blum, C. P. Dullemond, The outcome of protoplanetary dust growth: pebbles, boulders, or planetesimals? II. Introducing the bouncing barrier. *Astronomy & Astrophysics* **513**, A57 (2010).
68. S. J. Weidenschilling, The Origin of Comets in the Solar Nebula: A Unified Model. *Icarus* **127**, 290-306 (1997).
69. S. J. Weidenschilling, Formation of Planetesimals and Accretion of the Terrestrial Planets. *Space Science Reviews* **92**, 295-310 (2000).
70. F. Windmark, *et al.*, Planetesimal formation by sweep-up: how the bouncing barrier can be beneficial to growth. *Astronomy & Astrophysics* **540**, A73 (2012).
71. S. Okuzumi, H. Tanaka, H. Kobayashi, K. Wada, Rapid Coagulation of Porous Dust Aggregates outside the Snow Line: A Pathway to Successful Icy Planetesimal Formation. *The Astrophysical Journal* **752**, 106 (2012).
72. S. J. Desch, H. C. Connolly, Jr., A model of the thermal processing of particles in solar nebula shocks: Application to the cooling rates of chondrules. *Meteoritics and Planetary Science* **37**, 183-207 (2002).
73. F. J. Ciesla, L. L. Hood, S. J. Weidenschilling, Evaluating planetesimal bow shocks as sites for chondrule formation. *Meteoritics and Planetary Science* **39**, 1809-1821 (2004).
74. C. P. McNally, A. Hubbard, M.-M. Mac Low, D. S. Ebel, P. D'Alessio, Mineral Processing by Short Circuits in Protoplanetary Disks. *The Astrophysical Journal* **767**, L2 (2013).
75. I. S. Sanders, G. J. Taylor, *Chondrites and the Protoplanetary Disk*, A. N. Krot, E. R. D. Scott, B. Reipurth, eds. (2005), vol. 341 of *Astronomical Society of the Pacific Conference Series*, p. 915.
76. J. E. Chambers, G. W. Wetherill, Planets in the asteroid belt. *Meteoritics and Planetary Science* **36**, 381-399 (2001).
77. H. F. Levison, *et al.*, Contamination of the asteroid belt by primordial trans-Neptunian objects. *Nature* **460**, 364-366 (2009).

# Supplementary Materials

A. Johansen, M.-M. Mac Low, P. Lacerda, & M. Bizzarro

## 1 Materials and Methods

### 1.1 Sink particles in the Pencil Code

In order to track the masses of the planetesimals as they form and grow, we have developed a new sink particle module for the Pencil Code. Above a threshold particle density value  $\rho_p = \rho_p^{(\text{sink})}$  all particles in the cell are merged to a single sink particle. This sink particle does not feel friction with the gas, due to the large size of the planetesimal. Any particle coming within the distance  $\delta x/2$  of a sink particle is destroyed ( $\delta x$  is the size of the resolution element) and its mass and momentum added to the sink particle. In Figure S1 we compare the planetesimal masses arising from simulations at  $256^3$  with three different values for the sink particle creation threshold. The figure shows that the results are relatively unaffected by the choice of sink particle creation thresholds above 5 times the Roche density. Sink particles allow us to easily keep track of the temporal evolution and saturation of the planetesimal masses, and the merging of several million superparticles into a few sink particles prevents the simulation from slowing down when superparticles cluster on a subset of the available processors (56).

### 1.2 Chondrule accretion simulations

While classical simulations of planetesimal growth focus on the growth by gravitationally focused planetesimal-planetesimal collisions (20, 21, 57), the accretion of chondrule-sized objects coupled to the gas via friction can potentially be much more relevant if planetesimals are born and grow in an ocean of chondrules (23, 24, 58). “Chondrule accretion” is an aspect of the more general term “pebble accretion”, but chondrules are much smaller than the typically cm-sized pebbles used in previous studies of pebble accretion.

### 1.3 Pebble accretion

Pebble accretion has two dominant regimes. Planetesimals below a transition radius of around 1000 km (at 2.5 AU) accrete pebbles embedded in the sub-Keplerian gas. In the Minimum Mass Solar Nebula (19) the relative speed between a planetesimal on a circular orbit and the gas is  $\Delta v \approx 50$  m/s. These pebbles are accreted by the planetesimal from the Bondi radius of the planetesimal,

$$R_B = GM/(\Delta v)^2, \quad (6)$$

provided that the friction time of the pebble matches the time to cross the Bondi radius. Larger pebbles are simply scattered by the planetesimal, while smaller pebbles can not be pulled away quickly enough from the almost straight streamlines of the gas. The finite size of the planetesimal leads to additional complexities, namely gravitational focusing of loosely coupled pebbles; and the Stokes flow of the gas around the planetesimal, which affects the trajectories of strongly coupled particles with impact parameters similar to or smaller than the radius of the planetesimal.

In order to model all these effects correctly we have solved for the trajectories of a large number of pebble-planetesimal combinations, for different values of the friction time  $t_f$  and the planetesimal radius  $R$ . The planetesimal is kept stationary at  $(x, y) = (0, 0)$ , while the pebble moves under the influence of planetesimal gravity and gas drag. Pebbles enter the simulation domain at a large, positive value of  $x$  and with impact parameter  $b = y_0$ . The gas velocity field is kept fixed and follows the Stokes solution (59)

$$u_r = -\Delta v \cos(\theta) \left( 1 - \frac{3R}{2r} + \frac{1}{2} \frac{R^3}{r^3} \right), \quad (7)$$

$$u_\theta = +\Delta v \sin(\theta) \left( 1 - \frac{3R}{4r} - \frac{1}{4} \frac{R^3}{r^3} \right). \quad (8)$$

Here  $r$  and  $\theta$  are the polar coordinates, with  $r$  denoting the distance from the origin and  $\theta$  the angle between the  $x$ -axis and the  $y$ -axis, so that the gas flow at large  $r$  is uniform along the  $x$ -direction  $\mathbf{u} = -\Delta v \hat{x}$ . Collisions with the planetesimal are treated as instantaneous, conserving the total momentum as well as the speed component parallel to the surface and a fraction  $c$  of the speed component perpendicular to the surface, with  $c$  denoting the coefficient of restitution. The pebble is assumed to be

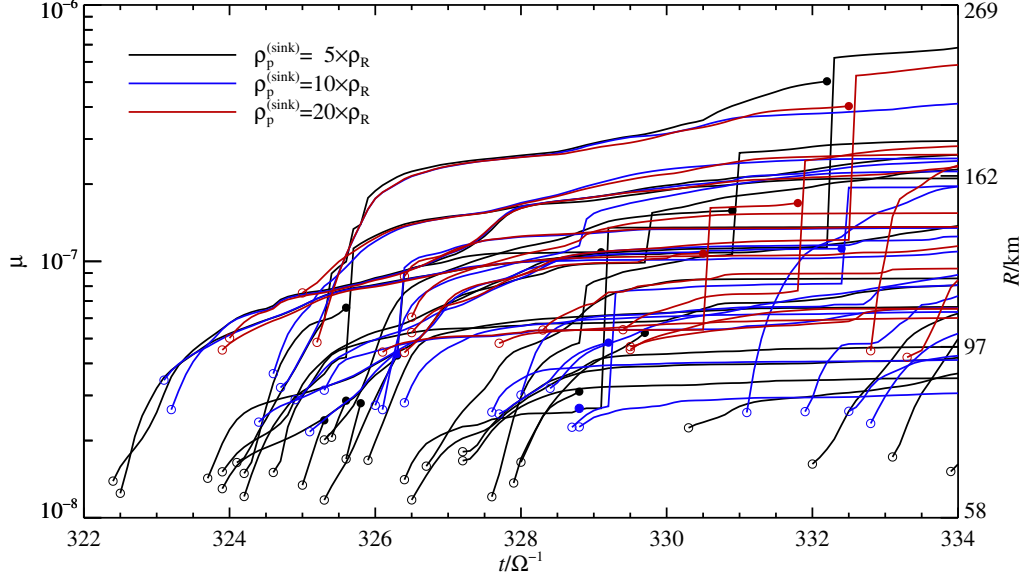


Figure S1: The non-dimensional planetesimal masses  $\mu = \rho_p(\delta x)^3$  (here  $\rho_p$  is the particle density represented by the planetesimal in a grid cell and  $\delta x$  is the size of the cell) and corresponding contracted radii as a function of time after self-gravity is turned on. Simulations at  $256^3$  grid cells and three different values of the sink particle creation threshold are compared. Creation of a planetesimal is marked with an empty circle, while the destruction is marked with a filled circle. The sizes of the largest planetesimals are relatively unaffected by the choice of the threshold. There are more mergers of small planetesimals at a low sink particle creation threshold, but the planetesimals resulting from those collisions correspond well to the massive planetesimals forming at higher creation thresholds.

accreted after colliding with the planetesimal 5 times or after orbiting the planetesimal 5 times. The latter criterion is convenient for planetesimals with large Bondi radii where the pebble enters a slowly decaying orbit around the planetesimal.

We show the accretion radius  $R_{\text{acc}}$  (the impact parameter required for accretion) for (a) perfect sticking and (b) a coefficient of restitution of  $c = 0.5$  in Figure S2. The accretion radius depends on both the friction time (normalised by the Bondi time  $t_B = R_B/\Delta v$  in Figure S2) and the planetesimal size (normalised by the Bondi radius). We discuss the general trends in the accretion radius curve here:

*Large Bondi radius.* The gas flow around the planetesimal and the coefficient of restitution play no role in determining the accretion radius when the planetesimal is much smaller than the Bondi radius. This is the case for large planetesimals and/or low relative pebble-planetesimal speeds. The three sections on the growth curve in Fig. S2 are: (i) Strong coupling when the pebble couples to the gas on a much shorter time-scale than the Bondi time-scale. Here the accretion radius is proportional to  $R_B\sqrt{t_f/t_B}$ . (ii) Weak coupling when the pebble couples to the gas on much longer time-scales than the Bondi time-scale. Here the accretion radius drops rapidly with increasing friction time, with no simple analytical expression. (iii) Gravitational focussing for the largest particles when the weak coupling branch drops below the gravitational focussing radius.

*Small Bondi radius.* A small planetesimal has Bondi radius much smaller than the planetesimal radius. This limit has two distinct branches: (i) Sedimentation overshoot for strongly coupled pebbles. These pebbles follow the Stokes flow around the planetesimal, but manage to sediment on to the surface for very low impact parameters where the gas flow comes very close to the planetesimal surface. (ii) Geometric accretion for weakly coupled pebbles that do not react to the modified gas flow close to the planetesimals. The latter branch in turn is strongly affected by the coefficient of restitution. Perfect sticking leads to accretion onto the entire projected surface, while consideration of the collision outcome requires very low impact parameters to remain bound after the collision.

Below we discuss some important aspects of the sedimentation overshoot and geometric branches.

*Sedimentation overshoot.* Small particles are carried with the gas around the planetesimals. The frictional acceleration between gas and particles is nevertheless not instantaneous but operates on the time-scale  $t_f$ . This can lead to accretion of particles that sediment onto the planetesimal surface during the transport around the planetesimal. The gas streamlines at a low impact

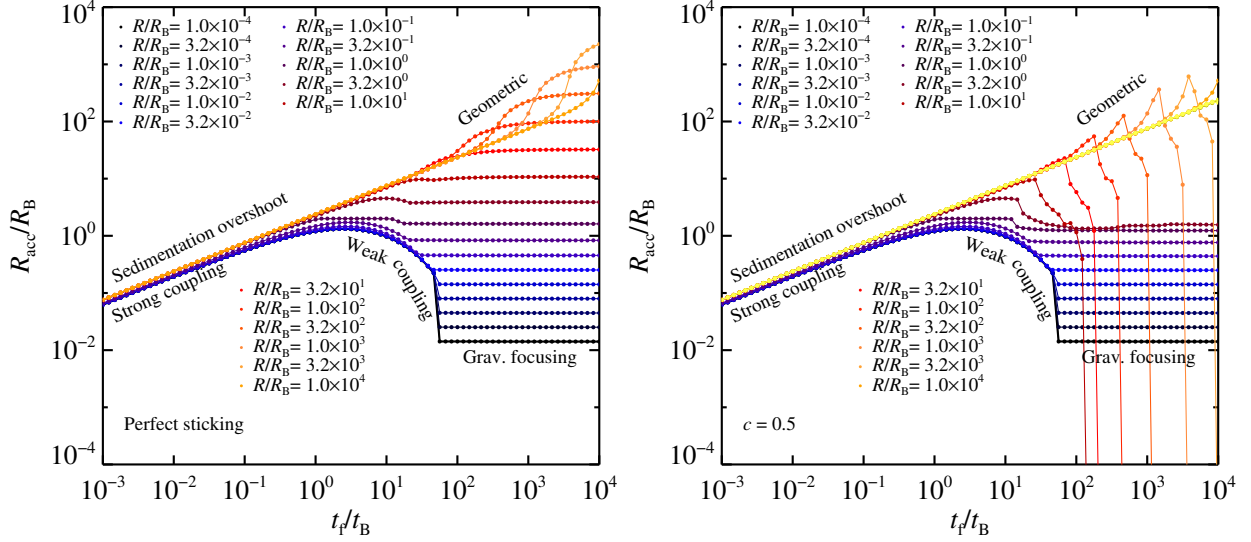


Figure S2: The accretion radius  $R_{\text{acc}}$  (i.e. the impact parameter required for accretion, given in units of the Bondi radius  $R_B$ ) versus the particle friction time  $t_f$  (in units of the Bondi time-scale  $t_B$ ), for planetesimal radii  $R$  between  $10^{-4}R_B$  and  $10^4R_B$ . The left panel shows the results when assuming perfect sticking between pebble and planetesimal. Planetesimals with  $R < R_B$  have three rather distinct branches: strong coupling for short friction times, weak coupling for longer friction times and finally gravitational focusing for the longest friction times. Planetesimals with  $R > R_B$  radius have two branches: sedimentation overshoot for short friction times (which follows the strong coupling scaling but is physically distinct) and geometric accretion for friction times longer than the time to pass the planetesimal. The consideration of the outcome of the pebble-planetesimal collision, with a coefficient of restitution  $c = 0.5$ , is shown the right panel. This strongly limits geometric accretion onto small planetesimals.

parameter of  $y_0 = b \ll R$  move around the planetesimal at the distance  $\delta r \sim b$ , at the approximate speed

$$u_\theta \sim \Delta v \frac{b}{R}. \quad (9)$$

Ignoring factors of order unity, the time to move around the planetesimal is then

$$\tau_\theta \sim \frac{R}{u_\theta} \sim \frac{R^2}{b\Delta v}. \quad (10)$$

During this time the pebble sediments towards the planetesimal at the terminal velocity

$$v_t = t_f \frac{GM}{R^2}. \quad (11)$$

The criterion for reaching the surface is  $v_t \tau_\theta \sim b$ . This in turn yields

$$b^2 \sim t_f \frac{GM}{\Delta v}. \quad (12)$$

Dividing by the squared Bondi radius finally yields the criterion for accretion

$$\frac{b^2}{R_B^2} \sim \frac{t_f}{t_B}. \quad (13)$$

This expression is equivalent to the strong coupling limit of pebble accretion (24), although the physics of the accretion via sedimentation overshoot is completely different.



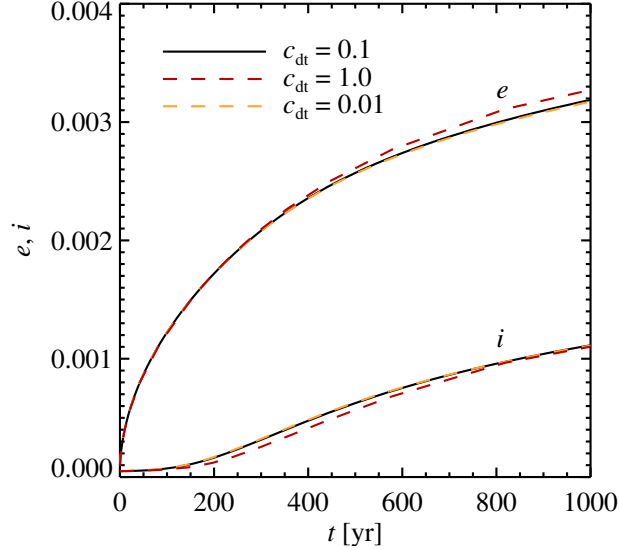


Figure S3: The evolution of eccentricity  $e$  and inclination  $i$  of 1000 planetesimals with mass  $M = 10^{24}$  g located at 1 AU with a surface density of  $10 \text{ g/cm}^2$ , for three values of the time-step. Here  $c_{\text{dt}}$  denotes the time-step relative to the collision time-scale. Stirring and dynamical friction are implemented using the scheme described in Ohtsuki et al. (2002). The results are qualitatively similar to Figure 4 of that paper, although the  $e$  and  $i$  evolve a bit slower in our simulation. We attribute this to a difference in the set up of the simulations: while we initially set  $e = 10^{-4}$  and  $i = 5 \times 10^{-4}$  for all planetesimals, Ohtsuki et al. (2002) give their planetesimals a Rayleigh distribution around those values. We use  $c_{\text{dt}} = 0.1$  in the actual planetesimal growth simulations.

*Geometric accretion.* The requirement that the pebble remains bound after the collision can be found geometrically as

$$R_{\text{acc}} = R \sqrt{\frac{(v_e/\Delta v)^2 - c^2}{1 - c^2}}. \quad (14)$$

Pebbles entering with an impact parameter less than  $R_{\text{acc}}$  are thus accreted, while pebbles with a larger impact parameter collide once with the planetesimal and then fly off to infinity. The accretion radius is only positive for  $c < v_e/\Delta v = \sqrt{2}R_{\text{B}}/R$ . Hence planetesimals with Bondi radii smaller than their size can not accrete pebbles which couple to the gas on time-scales longer than the time-scale to pass the planetesimal (unless  $c$  is extremely low).

## 1.4 Eccentricity and inclination

The growing asteroids experience mutual gravitational encounters that excite the eccentricities and inclinations of the population. This affects the pebble accretion rate since the relative speed between a planetesimal and the sub-Keplerian pebble flow changes with position in the orbit for non-zero eccentricities and inclinations.

The temporal evolution of the eccentricity  $e$  and the inclination  $i$  is calculated using the analytical approximations of Ohtsuki et al. (32), constructed to match the results of  $N$ -body simulations for both low and high eccentricities. The analytical evolution equations for  $e$  and  $i$  give the excitation as well as dynamical friction of a binned population of planetesimals. We show in Figure S3 the result of a test problem defined in Ohtsuki et al. Here we consider 1000 equal-mass planetesimals with initial eccentricity of  $10^{-4}$  and inclination of  $5 \times 10^{-5}$ . The evolution of  $e$  and  $i$  follows the general curve in Figure 4 of Ohtsuki et al., but the evolution is a bit slower. We attribute this to a difference in the tests. In Ohtsuki et al. the planetesimals are given a Rayleigh distribution of  $e$  and  $i$  initially, while we assign a constant value equal to the mean of that Rayleigh distribution. A similar test problem with 800 planetesimals is shown in Figure S4, with good agreement with Figure 2 of Stewart & Ida (60).

In principle we could use all the planetesimal particles in the code as natural bins and evolve each planetesimal with the dynamical excitation contribution from all other planetesimals. However, this would take unfeasibly long time to compute when there are millions of planetesimal particles. Instead we bin the planetesimals by their radius and consider the dynamical evolution of the smallest and largest planetesimal in each bin. Gravitational stirring is only considered between these anchor planetesimals. The resulting values of  $de^2/dt$  and  $di^2/dt$  are then multiplied by the total number of planetesimals in the stirring bin, divided

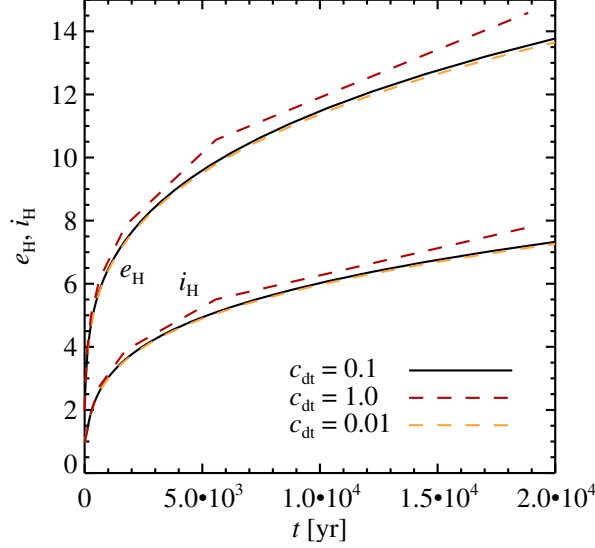


Figure S4: The evolution of eccentricity  $e$  and inclination  $i$  of 800 planetesimals with mass  $M = 10^{24}$  g located at 1 AU with a surface density of  $10 \text{ g/cm}^2$ . The eccentricity and the inclination are normalised by their Hill values  $[2M_p/(3M_\star)]^{1/3}$ . Results are qualitatively similar to Figure 2 of Stewart & Ida (2000). As in Figure S3, a time-step parameter of  $c_{dt} = 0.1$  provides a good compromise between precision and speed; hence we use  $c_{dt} = 0.1$  for planetesimal stirring in the planetesimal growth simulations.

by the number of planetesimals that were actually considered (the two anchors). The evolution of  $e$  and  $i$  is finally interpolated from the anchor planetesimals to all the other planetesimals at the end of the time-step.

The eccentricity and inclination of the orbit can now be used to calculate the pebble accretion rate over a full orbit of the planetesimal. For small eccentricities and inclinations the orbit can be considered in the local coordinate frame corotating with the Keplerian flow at a given distance  $r_0$  from the star. The coordinate system is oriented such that the  $x$ -axis points radially away from the star, the  $y$ -axis along the orbital direction of the gas and the  $z$ -axis perpendicular to the plane of the disk, along the rotation vector of the disk. The epicyclic motion of a planetesimal with eccentricity  $e$  in such a frame is

$$v_x(t) = v_e \cos(\Omega t), \quad (15)$$

$$v_y(t) = -\frac{1}{2}v_e \sin(\Omega t), \quad (16)$$

$$v_z(t) = v_i \cos(\Omega t). \quad (17)$$

Here  $v_e = ev_{K,0}$  and  $v_i = iv_{K,0}$  are the eccentricity and inclination speeds of the orbit, respectively, measured relative to the Keplerian speed at the centre of the frame, and  $(v_x, v_y)$  is the velocity is measured relative to the *local* Keplerian motion at the instantaneous position of the planetesimal. Relative to  $v_{K,0}$  the azimuthal velocity is

$$\tilde{v}_y(t) = -2v_e \sin(\Omega t). \quad (18)$$

The velocity of the incoming chondrules is  $v'_y = -\Delta v$  relative to the local Keplerian velocity. Hence the relative speed between planetesimal and chondrules is

$$v_{\text{rel}} = \sqrt{[v_e \cos(\Omega t)]^2 + [-(1/2)v_e \sin(\Omega t) + \Delta v]^2 + [v_i \cos(\Omega t)]^2}. \quad (19)$$

The relative speed is lowest at aphelion ( $\Omega t = \pi/2$ ) and highest at perihelion ( $\Omega t = 3\pi/2$ ). Since the Bondi radius scales as  $R_B \propto 1/v_{\text{rel}}^2$ , the eccentric motion strongly affects the accretion rate. On the strong coupling branch of pebble accretion one can nevertheless show that the eccentric orbit will not affect the mass accretion rate, because in fact the accretion rate is independent of  $v_{\text{rel}}$ ,

$$\dot{M}_{\text{SC}} \propto \frac{t_f}{t_B} R_B^2 v_{\text{rel}} \propto \frac{t_f}{GM/v_{\text{rel}}^3} \frac{G^2 M^2}{v_{\text{rel}}^4} v_{\text{rel}} \propto GM t_f. \quad (20)$$

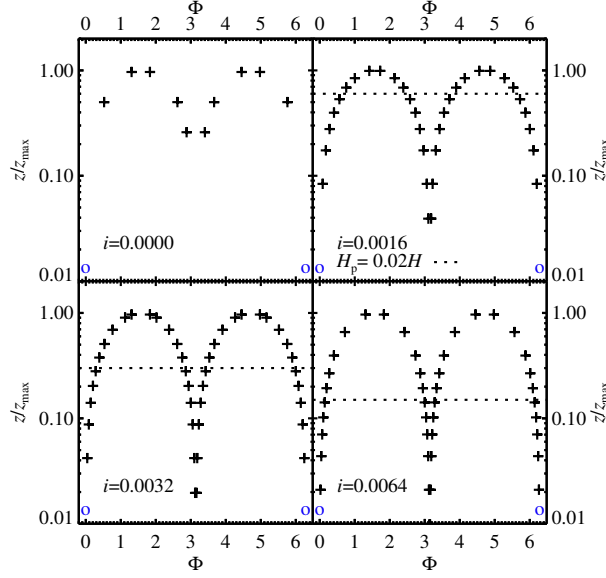


Figure S5: Phase points covering planetesimal orbits with inclinations  $i = 0$ ,  $i = 0.0016$ ,  $i = 0.0032$  and  $i = 0.0064$ . We construct phase arrays to cover both the full planetesimal orbit and the scale-height of the chondrule layer (here  $H_p = 0.02H$ ). The height in the planetesimal orbit is normalised by the maximum height for the given inclination. The dotted line indicates the scale-height of the chondrule mid-plane layer, clearly resolved for all choices of the inclination.

At aphelion the relative speed between chondrule and planetesimal can even approach zero for  $(1/2)v_e \sim \Delta v$ . At this point the Bondi radius is no longer the relevant accretion radius as the Hill speed of the planetesimal is higher than the relative chondrule-planetesimal speed, and the planetesimal thus enters short periods of Hill accretion at aphelion (our implementation of Hill accretion is explained in section 1.6).

We take into account the eccentric and inclined orbit of the planetesimal by sampling the accretion rate at a number of phases in the orbit. The choice of phase points is a balance between the need to sample both the scale height  $H_p$  of the chondrule layer, where chondrule densities are highest, as well as the planetesimal orbit over which the relative planetesimal-chondrule speed, and hence the accretion radius, varies. We set the first phase point at  $\Phi = \Omega t = 0$ . The distance to the next phase point is taken as the minimum of the two functions

$$\Delta\Phi_1 = \frac{\exp(z/H_c)H_c}{z_{\text{orb}}} \frac{2\pi}{N_1}, \quad (21)$$

$$\Delta\Phi_2 = \frac{2\pi}{N_2}. \quad (22)$$

Here  $z_{\text{orb}}$  is the maximal height of the planetesimal relative to the mid-plane. This gives phases that cover the full planetesimal orbit, with additional resolution elements added within the chondrule scale height. This way we avoid having to use a very large number of points for highly inclined orbits. We show examples of phase arrays in Figure S5 for  $N_1 = 48$  and  $N_2 = 12$ .

In Figure S6 we show the mass accretion rate of planetesimals at 2.5 AU as a function of the eccentricity of the orbit. We use the approximation that  $i = e/2$  and measure the accretion rate relative to that at  $e = i = 0$ . Increasing the eccentricity actually increases the geometric accretion rate on small planetesimals (below 50 km in radius), since the relative planetesimal-chondrule speed increases and hence the mass flux increases proportionally to the speed. Larger planetesimals are affected negatively by eccentricity. These planetesimals accrete small chondrules at very high rate on circular orbits. The accretion rate at the aphelion of an eccentric orbit does not benefit strongly from the decreased relative planetesimal-chondrule speed at that phase, since the larger Bondi radius requires very large chondrules, which are not present in the disk. Instead the planetesimal enters the strong coupling branch at aphelion, while the accretion rate is strongly reduced at perihelion. The overall result is a reduction in the accretion rate. Even larger planetesimals are affected less and less by the increase in eccentricity. These large planetesimals already accrete on the strong coupling branch, which is relatively unaffected by the relative speed and hence by the eccentricity.

Figure S7 illustrates the mass accretion rates of planetesimals at 25 AU for different values of their eccentricity. The normalised accretion rates in Figure S7 are flat or increasing beyond 200 km in radius, indicating a very steep increase in the accretion rate

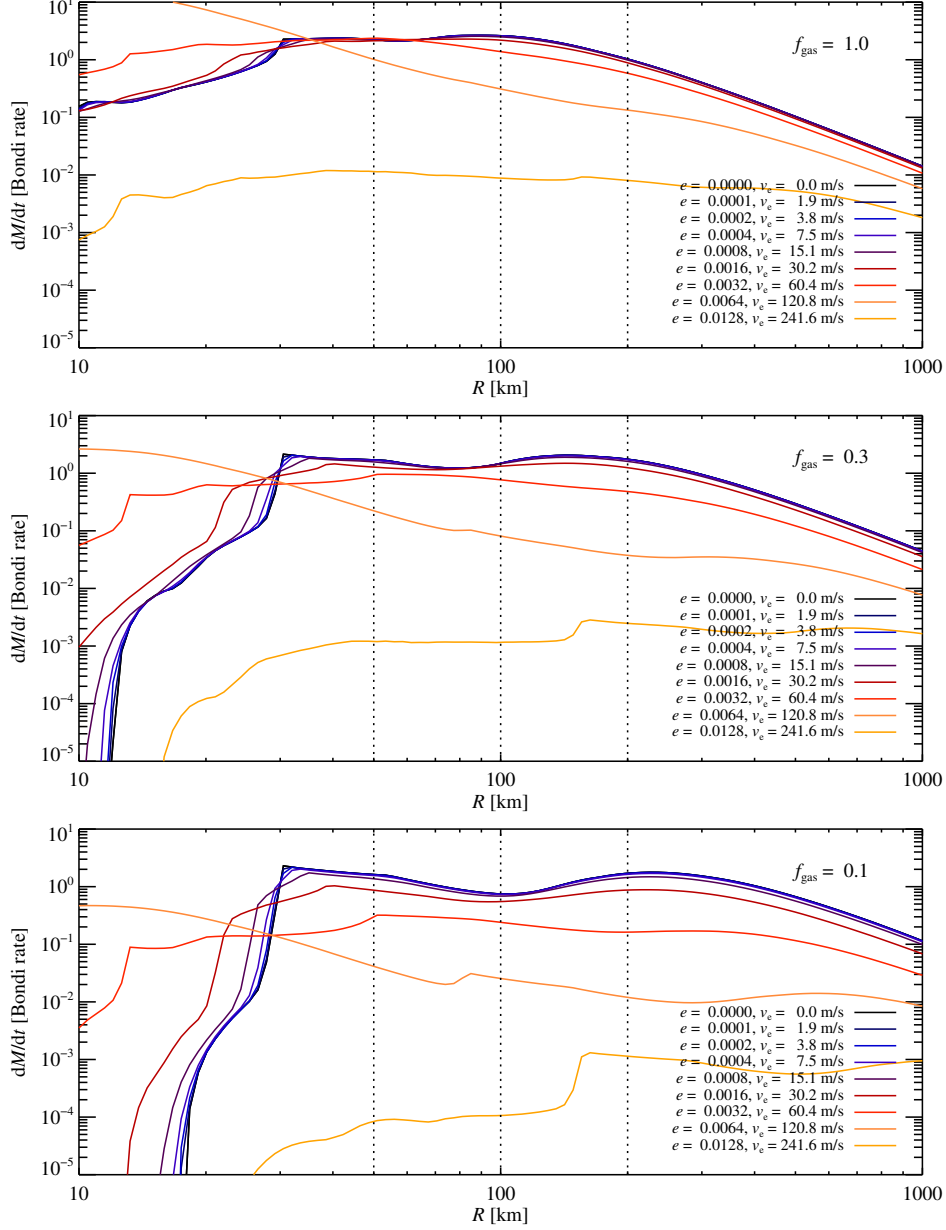


Figure S6: The effect of eccentricity and inclination on the chondrule accretion rate, at an orbital distance of 2.5 AU. The  $x$ -axis shows the planetesimal sizes and the  $y$ -axis the pebble accretion rate normalised to the accretion rate from the full Bondi radius. Dotted lines mark 50 km, 100 km and 200 km. We use here the approximation  $i = e/2$ . Increasing the orbital eccentricity can actually increase the accretion rate on bodies smaller than 100 km in radius, as the orbital speed in aphelion matches the sub-Keplerian speed of the chondrules which leads to very high accretion rates. Larger planetesimals are affected negatively beyond the threshold  $(e/2)v_K = \Delta v$  as the large particles necessary for efficient accretion at aphelion are not present in the disk. The top plot shows results for the column density of the Minimum Mass Solar Nebula at 2.5 AU, the middle plot 0.3 times the MMSN and the bottom plot 0.1 times the MMSN.

with size. This is in contrast to the situation in the asteroid belt where the run-away accretion of chondrules is stopped by the lack of chondrules larger than mm in size (Figure S6).

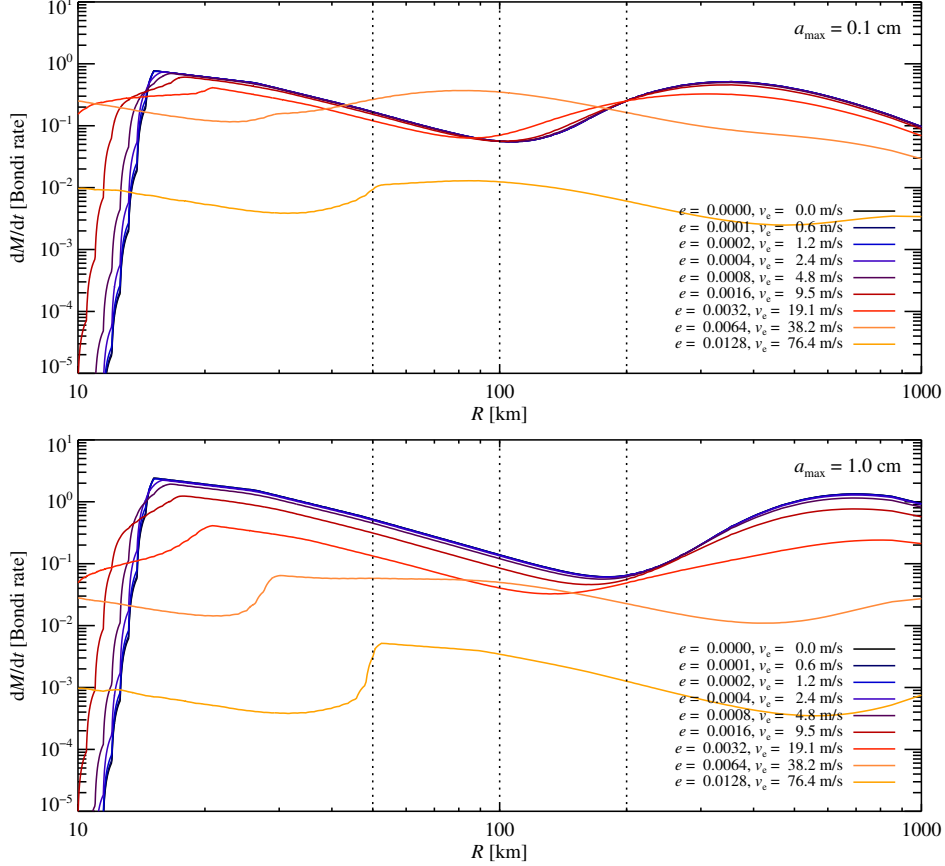


Figure S7: The accretion rate of planetesimals at 25 AU, as a function of the planetesimal size. The accretion rate is normalised by the Bondi rate. The top panel shows the accretion rate for pebbles up to 1 mm in radius, while the bottom panels shows the accretion rate for pebbles up to 1 cm in radius. The accretion rate beyond 200 km in radius is flat or increasing here in the outer regions of the protoplanetary disk. This is in contrast to the situation in the asteroid belt where the lack of chondrules of larger than mm size slows down the run-away accretion of large planetesimals (Figure S6). The presence of mm-cm pebbles in the outer protoplanetary disk can drive a run-away accretion where the most massive planetesimals detach from the rest of the population (see Figure 10).

## 1.5 Stratification integral

Calculation of the mass accretion rate requires knowledge of the accretion radius as well as the chondrule density averaged over the accretion radius. The stratification integral  $S$  is defined as the mean chondrule density normalised by the chondrule density in the mid-plane. The stratification integral for a planetesimal with accretion radius  $R_{\text{acc}}$  located at the height  $z_0$  over the mid-plane is

$$S = \frac{1}{\pi R_{\text{acc}}^2} \int_{z_0 - R_{\text{acc}}}^{z_0 + R_{\text{acc}}} \exp[-z^2/(2H_p^2)] 2\sqrt{R_{\text{acc}}^2 - (z - z_0)^2} dz. \quad (23)$$

This expression is obtained by summing over lines of constant  $z$  and hence constant chondrule density. There is no simple analytical solution to equation (23). Tabularisation of the numerical solution requires interpolation in both  $R_{\text{acc}}$ ,  $z_0$  and the angle of incidence of the chondrule flow  $\theta$  (see below). We therefore an approximation that allows the integral to be calculated analytically. This *square* approximation integrates the chondrule density over a square instead of a circle. This yields the solvable integral

$$S_{\text{square}} = \frac{1}{4R_{\text{acc}}^2} \int_{z_0 - R_{\text{acc}}}^{z_0 + R_{\text{acc}}} \exp[-z^2/(2H_p^2)] 2R_{\text{acc}} dz. \quad (24)$$



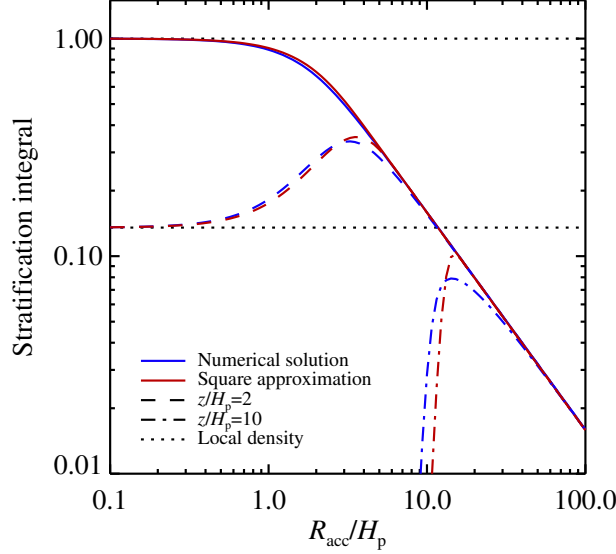


Figure S8: The stratification integral (i.e., the mean particle density over the accretion cross section) as a function of the accretion radius of the planetesimal. Numerical integration of the Gaussian stratification over a circle (blue lines) is expensive, so we use instead a square approximation to the integral (red lines). Full lines indicate a planetesimal in the mid-plane, dashed lines a planetesimal at two times the chondrule scale-height above the mid-plane, and dash-dotted lines a planetesimal at ten times the chondrule scale-height. The square approximation is very precise both when the accretion radius is much lower or much higher than the chondrule scale-height.

The analytical solution is

$$S_{\text{square}} = \frac{H_p}{\sqrt{2}R_{\text{acc}}} \frac{\sqrt{\pi}}{2} \left[ \text{erf} \left( \frac{z_0 + R_{\text{acc}}}{\sqrt{2}H_p} \right) - \text{erf} \left( \frac{z_0 - R_{\text{acc}}}{\sqrt{2}H_p} \right) \right]. \quad (25)$$

The square approximation tends to underestimate the chondrule density because of the inclusion of low-density corners in the square. Therefore we decrease the size of the square by replacing  $R_{\text{acc}}$  in equation (25) with  $R'_{\text{acc}} = fR_{\text{acc}}$ . We have found  $f = 0.79$  to give a much better fit to the numerical integral than  $f = 1$ . In Figure S8 we show how the square approximation compares to the full numerical integration of the accretion radius over the Gaussian stratification.

Planetesimals at very high inclinations encounter the chondrule flow at an angle  $\theta$  which is  $\neq 0^\circ$ , measured relative to the vertical. The angle of incidence is found through

$$\theta = \text{acos} \left( \frac{v_z^{(\text{rel})}}{v_{\text{rel}}} \right) \quad (26)$$

Here  $v_{\text{rel}} = |\mathbf{v}_{\text{rel}}| = |\mathbf{v}_p - \mathbf{v}_c|$  is the vectorial relative speed between the planetesimal (with velocity  $\mathbf{v}_p$ ) and the chondrules (with velocity  $\mathbf{v}_c = -\Delta v \hat{\mathbf{y}}$ ). The components of  $\mathbf{v}_p$  are given in equations (15)-(17). The consideration of the angle of incidence changes the stratification integral to

$$S = \frac{1}{\pi R_{\text{acc}}^2} \int_{z_0 - R_{\text{acc}} \cos \theta}^{z_0 + R_{\text{acc}} \cos \theta} \exp[-z^2/(2H_p^2)] 2\sqrt{R_{\text{acc}}^2 - \left( \frac{z - z_0}{\cos \theta} \right)^2} \frac{dz}{\cos \theta}. \quad (27)$$

The square approximation changes to

$$S_{\text{square}} = \frac{H_p}{\sqrt{2}R_{\text{acc}}} \frac{\sqrt{\pi}}{2} \frac{1}{\cos \theta} \left[ \text{erf} \left( \frac{z_0 + R_{\text{acc}} \cos \theta}{\sqrt{2}H_p} \right) - \text{erf} \left( \frac{z_0 - R_{\text{acc}} \cos \theta}{\sqrt{2}H_p} \right) \right]. \quad (28)$$

The results presented in this paper are obtained with the square approximation including the correction for the encounter angle.

## 1.6 Transition to Hill accretion

Bondi accretion is only valid for planetesimals below a transition mass of approximately 0.1% of an Earth mass (24). Beyond this the Hill radius of the growing planetesimal,  $R_H$ , is so large that the relative speed between chondrule and planetesimal is set by the Hill speed  $v_H = \Omega R_H$  rather than the sub-Keplerian speed  $\Delta v$ .

We obtain a smooth transition from Bondi accretion to Hill accretion by solving for the combined speed  $v(R_{\text{acc}}) = \Delta v + \Omega R_{\text{acc}}$ . The accretion radius  $R_{\text{acc}}$  depends on the approach speed, so we solve the equation iteratively from the starting point  $v = \Delta v$ . This allows us to also apply the tabulated accretion radius for Bondi accretion (Figure S2) to Hill accretion, by modifying the approach speed to take into account the Keplerian shear. We have checked that the resulting accretion rates on the Hill branch are very similar to the results from hydrodynamical simulations (24).

## 1.7 Eccentricity damping by gas drag and chondrule accretion

The planetesimals in our model are so large that the quadratic drag force regime applies, with drag force proportional to the relative speed squared and with friction time

$$t_f = \frac{6R\rho_\bullet}{\delta v\rho_g}. \quad (29)$$

The drag force can be applied directly to the eccentricity and inclination, following Wetherill & Stewart (1989) (61) and Morbidelli et al. (2009) (21),

$$\frac{de^2}{dt} = -\frac{16}{5} \frac{v}{v_K^2} \frac{0.5\pi\rho_g v_g^2 R^2}{2M(1+0.8\beta^2)}, \quad (30)$$

$$\frac{di^2}{dt} = -3.2\beta^2 \frac{v}{v_K^2} \frac{0.5\pi\rho_g v_g^2 R^2}{2M(1+0.8\beta^2)}. \quad (31)$$

Here we use the notation of Morbidelli et al. (2009) who define  $\beta = i/e$ ,  $v = v_K\sqrt{(5/8)e^2 + (1/2)i^2}$  and  $v_g = \sqrt{v(v + \Delta v)}$ . This formulation damps the eccentricity and inclination to zero on the relevant friction time-scale, with the term  $v + \Delta v$  in  $v_g$  corresponding to an orbitally averaged relative speed which would enter equation (29). We have checked the analytical evolution of  $e$  and  $i$  against an  $N$ -body integration of an eccentric orbit circularised by gas drag and found excellent agreement.

Chondrule accretion and scattering are two additional damping mechanisms. The friction time-scale for chondrule accretion with accretion radius  $R_{\text{acc}}$  is

$$t_{f,\text{cho}} = \frac{M}{\pi R_{\text{acc}}^2 \rho_p \delta v} = \frac{4}{18} \frac{R^2}{R_{\text{acc}}^2} \frac{\rho_g}{\rho_c} t_{f,\text{gas}}. \quad (32)$$

We use similar expressions to equations (30)-(31) for the damping by chondrule accretion, but with  $R^2$  replaced by  $R_{\text{acc}}^2$ ,  $\rho_g$  replaced by  $\rho_p$ , and multiplied by 18/4 to take into account that the pre-factor in the friction time of chondrule accretion (4/3) is much lower than for gas drag (6). Damping by bouncing collisions and chondrule scattering is taken into account by using the maximum of the Bondi radius and the physical radius as the gravitational interaction radius when  $t_f > t_B$  and  $R_{\text{acc}} < R$ .

## 1.8 Planetesimal growth simulations

The dynamical equations describing the temporal evolution of the masses, eccentricities and inclinations of a large number of planetesimals are solved in a numerical code named ‘‘Pebble Accretion Onto Planetesimals and Planets’’ (PAOPAP), which we have developed for the purpose of demonstrating the importance of chondrule accretion for planetesimal growth. Information about the simulations can be also found in the main paper; here we give some additional details.

The planetesimals are treated as individual particles in the code, each represented by a mass, an eccentricity and an inclination. Planetesimal masses are evolved via the accretion of chondrules and mutual planetesimal collisions (see Section 1.9), while the eccentricities and inclinations are changed by both viscous stirring and dynamical friction from the other planetesimals, as well as damping by gas drag and pebble accretion and scattering. We ignore mass erosion of small ( $< 50$  km) planetesimals by large chondrules impacting and bouncing at super-escape speeds.

The code divides the planetesimals into discrete size bins and calculates  $\dot{M}$ ,  $\dot{e}$  and  $\dot{i}$  for the smallest and largest planetesimal in each bin. The temporal evolution of all other planetesimals is found by interpolation from the two anchors in each bin. This approach allows us to simulate a high number of planetesimals at a relatively low computational cost and to resolve the run-away growth of a small number of large objects. We use 200 logarithmically spaced bins spanning from 10 km to 10,000 km in radius.

The chondrule density has a Gaussian stratification profile, with the scale-height  $H_p$  in each bin set according to the diffusion-sedimentation equilibrium expression

$$\frac{H_c}{H_g} = \sqrt{\frac{\alpha}{\Omega t_f + \alpha}}. \quad (33)$$

Here  $H_g$  is the gas scale-height,  $\alpha$  is the turbulent viscosity (which we assume takes the same value as the turbulent diffusion coefficient),  $\Omega$  is the Keplerian frequency at the orbital distance to the asteroid belt and  $t_f$  is the friction time. The latter is given in the Epstein regime by

$$t_f = \frac{a\rho_\bullet}{c_s\rho_g}, \quad (34)$$

with  $a$  denoting the particle radius,  $\rho_\bullet$  the material density,  $c_s$  the sound speed in the gas (which depends only on the temperature and the mean molecular weight), and  $\rho_g$  the gas density. We choose a nominal turbulent diffusion coefficient of  $\alpha = 10^{-4}$  (we discuss this choice in the main paper). This yields a scale-height of mm-sized particles of approximately 30% of the gas scale-height, with smaller particles having scale-heights increasing as the square root of their size.

We create chondrules continuously on a time-scale of 1.5 Myr to satisfy the cosmochemical evidence that chondrules in individual chondrites have ages from 0 to 3 Myr (5). We have performed test simulations where all the chondrules are present from the beginning; this accelerates chondrule accretion but does not affect the overall picture that asteroids, Kuiper belt objects and planetary embryos grow by chondrule accretion. The chondrules are divided into 30 logarithmically spaced bins, with the number density  $n(a)$  distributed according to the size distribution  $dn(a)/da \propto a^{-3.5}$ .

The planetesimals have initial sizes from 10 to 150 km, distributed in a shallow power law with the differential number following  $dN/dR \propto R^{-2.8}$ , but truncated with an exponential term  $\exp[-(R/R_{\text{exp}})^4]$  at the planetesimal radius  $R_{\text{exp}}=100$  km. The smallest planetesimals experience very little growth and act mainly to provide dynamical friction, damping the inclinations and eccentricities of the larger asteroids and planetary embryos.

The pebble accretion rates of the planetesimals are found via interpolation in a look-up table that gives the accretion radius for a grid of values of the planetesimal size  $R/R_B$  (normalised by the Bondi radius) and the chondrule friction time  $t_f/t_B$  (normalised by the Bondi time). The look-up table is based on a high number of integrations of the dynamics of single chondrules passing by a planetesimal with the sub-Keplerian flow.

The temporal integration of the dynamical equations is done via a simple Eulerian scheme, with the time-step determined to make  $M$ ,  $e$  and  $i$  change by a maximum of 10%. We experimented with 30% and found significant changes to the results, while 3% gives very similar results.

## 1.9 Planetesimal collisions

Planetesimal collisions are included in the code via a Monte Carlo method. The planetesimal particles are first sorted in discrete size bins. For each bin we calculate the average inclination and eccentricity of the planetesimals. We then calculate the collision rate matrix for all combinations of bins,  $r_{ij}$ . The collision rates are calculated following the scheme described in the online supplement of Morbidelli et al. (2009) (21). We refrain from describing the scheme in detail here since it is already well described in Section 1.1 of the online supplement of Morbidelli et al. (2009) (21).

From the time-step of the code we can then calculate the probability  $P_{ij}$  that a planetesimal from bin  $i$  collides with any of the planetesimals in bin  $j$  during the time-step. If a random number  $r$  is less than  $P_{ij}$  then the planetesimals will be collided. We assume perfect sticking between planetesimals and add the mass of the smaller planetesimal to the larger, removing afterwards the smaller planetesimal from the simulation.

We tested the coagulation scheme against an analytical solution to the coagulation equation where the kernel is constant (62). This corresponds to setting the collision rate  $r_{ij} = Kn_j$ , where  $K$  is a constant and  $n_j$  is the number density of planetesimals in bin  $j$ . The solution to the constant kernel test is that the number of bodies remaining at time  $t$  is

$$f = \frac{n(t)}{n_0} = \frac{1}{1 + Kn_0t/2}. \quad (35)$$

The number of remaining bodies versus time is shown in Figure S9, for different values of the time-step. The time-step is set by

$$dt = c_{dt}t_{\text{coll}}, \quad (36)$$

where  $t_{\text{coll}}$  is the collision time-scale and  $c_{dt}$  is a constant time-step parameter. There is excellent agreement in Figure S9 between the analytical expression and the results of the coagulation algorithm, for  $c_{dt} < 0.5$ . Passing this test implies that the Monte Carlo collision detection scheme is implemented correctly.

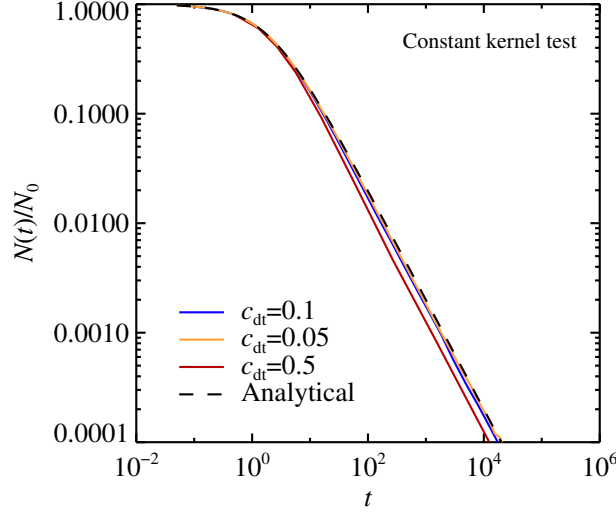


Figure S9: The number of remaining bodies versus time for the constant kernel test. There is an excellent agreement between the results of the coagulation algorithm and the analytical solution for a time-step parameter below  $c_{dt} = 0.5$ . The time-step parameter is the ratio of the time-step to the collision time-scale.

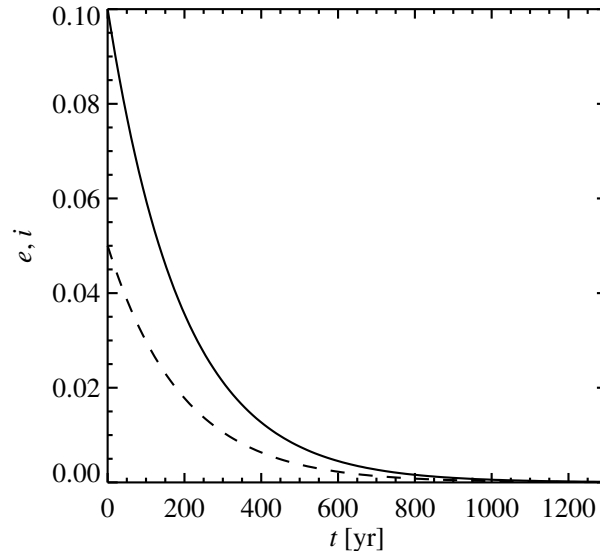


Figure S10: Damping of eccentricities and inclinations of 10,000 1-cm-sized planetesimals located between 30 and 35 AU, emulating a test problem defined in Morbidelli et al. (2009) (21). The total mass of the planetesimals is set to 10 Earth masses. The curves agree to within 15% with those shown in Figure 12 of the supplemental material of Morbidelli et al. (2009).

A test of the collision rate calculation can not be done as simply, as the expressions used in Morbidelli et al. (2009) (21) are complex. We choose therefore to reproduce one of the figures in that paper, namely a plot of the damping of eccentricities and inclinations of planetesimals due to mutual inelastic collisions. The damping is not very relevant for the large planetesimals considered in this paper, but the exact shape of the damping provides an excellent comparison with the collision rate calculation of Morbidelli et al. (2009) (21). The test problem considers 10 Earth masses of 1-cm-sized “planetesimals” located between 30 and 35 AU. Collisions are assumed to be inelastic and lead to energy dissipation; accretion and fragmentation are not included. Figure S10 shows the evolution of the eccentricity (initially 0.1) and the inclination (initially 0.05). There is agreement to within 15% between this plot and supplemental Figure 12 of Morbidelli et al. (2009) (21). This shows that the collision rate algorithm

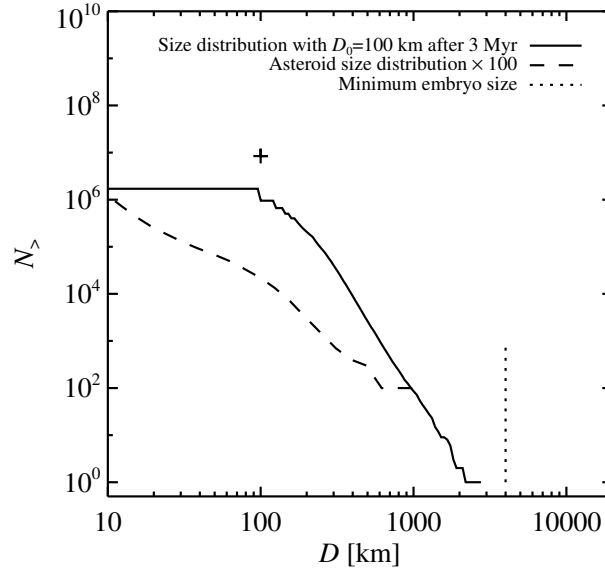


Figure S11: Cumulative size distribution after 3 Myr of coagulation within a population of planetesimals of initial diameters 100 km (50 km in radius), as shown by the cross. The size distribution is much steeper than the current observed size distribution in the asteroid belt. The results presented here are agree to within a few percent with Figure 5 of Morbidelli et al. (2009) (21) and Figure 5 of Weidenschilling (2011) (57), except for  $D > 1000$  km where we have a slight underproduction of embryos. Note that we set the column density of planetesimals equal to that of solids in the Minimum Mass Solar Nebula of Hayashi (1981), while Weidenschilling (2011) uses approximately twice that value.

is likely implemented properly in the PAOPAP code.

An additional test was performed with actual planetesimals. The evolution of a population of 50-km-radius planetesimals was presented in Figure 5 of Morbidelli et al. (2009) (21) and Figure 5 of Weidenschilling (2011) (57). We performed a similar simulation with our planetesimal accretion code. The resulting cumulative size distribution is shown in Figure S11. The cumulative size distribution is very steep and terminates just before reaching embryo sizes. This steep cumulative size distribution agrees to within a few percent with the results of Morbidelli et al. (2009) (21) and Weidenschilling (2011) (57), except for a slightly smaller production of the very largest embryos in our simulations. Note that these authors include fragmentation of planetesimals in their calculations, while we ignore this effect. The agreement of the results for  $D > 20$  km shows that planetesimal fragmentation plays little role for the coagulation of such large planetesimals. It is well-known that planetesimals larger than 100 km are strong and can survive high collision speeds (20).

## 2 Supplementary Text

### 2.1 Planetesimal formation in the asteroid belt

The particle sizes used in our streaming instability simulations correspond to approximately 25-cm-sized rocks at 2.5 AU in the Minimum Mass Solar Nebula (Stokes number  $St = 0.3$ ). This is much larger than the typical diameters of chondrules. We have chosen to study the formation of planetesimals from such large particle sizes in order to have a clean convergence test in parameters employed in previous works (13, 14). We suggest three ways to understand the actual formation of planetesimals in the asteroid belt:

1) *Chondrule aggregates*. Chondrules are covered with rims of fine-grained matrix (4) and these rims can facilitate the formation of chondrule aggregates. If the turbulent speed of the gas is very low, with turbulent viscosity  $\alpha \sim 10^{-6}$ , then collision speeds between rimmed chondrules are low enough to allow chondrules to stick together (17). The porous rims act as shock absorbers and facilitate the formation of decimeter-sized chondrule aggregates. These aggregates are large enough to trigger streaming instabilities and the direct formation of planetesimal seeds that can go on to accrete individual chondrules, as envisioned in the main paper. The radial drift speed of these aggregates is high, approximately 10 m/s, causing the aggregates to drift inwards within a few thousand years (63). The combination of growth and drift provides a means (a) to form planetesimals from such aggregates and (b) to subsequently flush these aggregates towards the inner solar system, to avoid feeding chondrule aggregates to the largest planetesimals, as this would trigger a very efficient run-away growth of asteroids and give a too steep size distribution.

2) *Large chondrules*. Another possibility is that the first planetesimal seeds formed out of centimeter-sized macrochondrules (16). These could have drifted out of the asteroid belt subsequent to planetesimal formation and left the stage for accretion of their millimeter-sized counterparts. Carrera, Johansen, & Davies (45) investigate the ability for the streaming instability to form dense filaments in particles down to chondrule sizes. While chondrule-sized particles are very hard to concentrate, particles just a few times larger (Stokes number of 0.01) concentrate readily into filaments at a particle mass loading of a few times the nominal value in the solar protoplanetary disk ( $Z_{\odot} \sim 0.01$ ). Here we explore whether these conditions are susceptible to planetesimal formation, by including the self-gravity between centimeter-sized particles (Stokes number of 0.01, so 30 times smaller than in the simulations presented in Figure 3 of the main paper). We use 2-D shearing sheet simulations and set the mean particle density to 1, 3 and 10 times the gas density, respectively, to mimic the mid-plane conditions seen in Carrera, Johansen, & Davies (45). The results are shown in Figure S12. The simulations with particle density  $\rho_p = 3\rho_g$  and  $\rho_p = 10\rho_g$  form a single planetesimal after a few hundred years. These planetesimals have a characteristic radius of approximately 100 km. This shows that planetesimals can indeed form out of particles as small as 1 cm in size and that the resulting planetesimal sizes are similar to those seen in Figure 3 of the main paper. Thus we show that asteroids can form from centimeter-sized particles. The full exploration of the relevant parameters for formation of planetesimals from centimeter-sized particles is beyond the scope of this paper, but this should have a high priority in future research.

3) *Icy pebbles*. It is possible that the ice line in the solar protoplanetary disk was much closer to the star in the earliest phases of protoplanetary disk evolution. Hence the asteroid belt could have been populated originally with icy pebbles of sizes comparable to what we used in the simulations (64). The first generation of icy asteroid seeds could subsequently have dried out after heating by  $^{26}\text{Al}$  or simply have been swamped in the subsequent accretion of dry chondrules. Carbonaceous chondrites display a wide range in their degree of aqueous alteration, consistent with the accretion and subsequent melting of icy pebbles (3). However, even some ordinary chondrites have been shown to have experienced water flows (65); and hence the formation of the seeds of the nowadays dry ordinary chondrites could have involved accretion of icy material.

Irrespective of the details of asteroid formation, the important factors for our chondrule accretion model are (i) planetesimals form, (ii) the planetesimals are not too small to prevent significant chondrule accretion, and (iii) planetesimals are not so large that all chondrules are accreted on the largest objects in the population. The computer simulations of planetesimal formation by streaming instabilities inspire us to take asteroid seeds with characteristic radii of 100 km and with a fairly shallow size distribution that puts most of the mass in the largest bodies.

### 2.2 Particle growth and chondrule precursors

In our model we assume that the centimeter-to-decimeter-sized particles discussed in the previous section were only present during the earliest stages of planet formation when the planetesimals formed. Ice particles could only exist while the ice line was interior of the asteroid belt, while the formation of chondrule aggregates requires very weak turbulence of  $\alpha \sim 10^{-6}$  (17), which may have required an extensive dead zone in a young (and hence still massive) protoplanetary disk. In this section we discuss why the later stages of the protoplanetary disk were likely dominated by chondrule-sized particles.

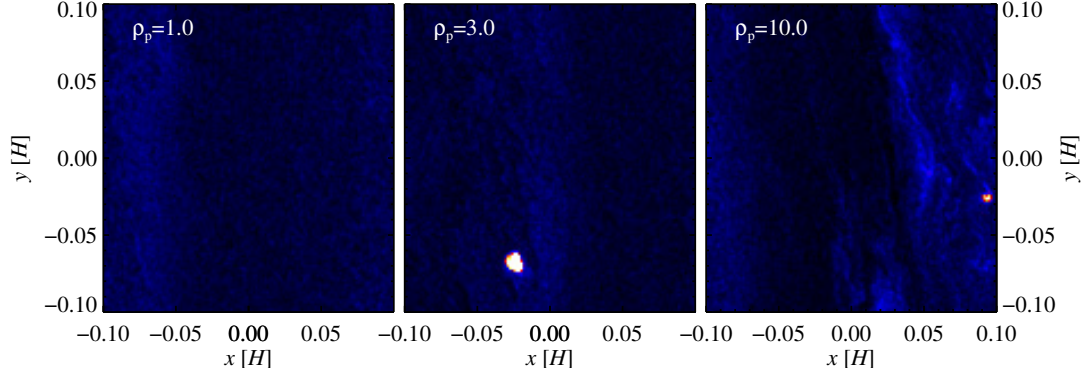


Figure S12: Formation of planetesimals from centimeter-sized particles in a 2-D shearing sheet simulation with the same spatial extent as the streaming instability simulations presented in the main text. The mean particle density is  $\rho_p = 1$  in the left panel,  $\rho_p = 3$  in the middle panel and  $\rho_p = 10$  in the right panel (relative to the gas density). The mean density is set to mimic the effect of both stratification and filament formation by the streaming instability. The simulations with  $\rho_p = 3$  and  $\rho_p = 10$  form a single, large planetesimal of approximately 100 km in radius after a few hundred years of integration. This numerical experiment shows that planetesimals can form for particle sizes corresponding to centimeter-sized macrochondrules and that planetesimal sizes are similar to those forming out of 25-cm-sized particles presented in Figure 3 of the main text.

The growth of dust particles in protoplanetary disks happens initially through sticking collisions that lead to the formation of fluffy dust aggregates; see the review paper on coagulation and planetesimal formation by Johansen et al. (1). These aggregates are compactified by mutual collisions as they reach approximately millimeter sizes. Compact dust aggregates have poor sticking properties and bounce off each other when they collide (66). This *bouncing barrier* is a major obstacle for dust growth (67), which could otherwise continue to much larger sizes (68, 69). Particles can still grow by mass transfer in high-speed collisions; however the growth rates remain too low to compete against radial drift (70). Another possibility is that ice particles could be extremely fluffy and experience perfect sticking even at high speeds (71). This nevertheless requires aggregates to consist of very small monomers ( $0.1 \mu\text{m}$ ), while matrix in chondrites is typically at least 10 times larger.

Hence it appears that the growth of silicate dust grains in the asteroid formation region stops at around mm sizes. This bouncing barrier picture fits well with the sizes of chondrules found in chondrite meteorites. The actual formation process of chondrules is highly uncertain, but is believed to involve heating of dust aggregate precursors in shocks (72, 73), in current sheets (74) in the protoplanetary disk or in impacts between molten planetesimals (75). Our model does not include the presence of chondrule precursors. Such precursors could have a low fractal dimension and hence low friction time, which would prevent sedimentation and efficient incorporation into the asteroids and embryos that grow in the mid-plane. Nevertheless the inclusion of chondrule precursors would not change the conclusions of our paper, as they would simply lead to a slightly higher accretion rate for asteroids and embryos.

### 2.3 Depletion of the asteroid belt

The current mass of the asteroid belt is only approximately  $5 \times 10^{-4}$  Earth masses. This contrasts with the extrapolation of the Minimum Mass Solar Nebula into the asteroid belt, which yields a particle column density of  $4.3 \text{ g/cm}^2$  and hence a primordial mass of 0.86 Earth masses. The depletion of the asteroid belt has happened mainly through collisional grinding and pumping of the eccentricity of asteroids in resonances with Jupiter. Based on a number of arguments, including the extant number of asteroid families and the number of large craters on Vesta, Bottke et al. (20) concluded that the collisional activity in the asteroid belt, after excitation of the asteroids to their current eccentricities, can not have been much larger than the current collision rate over 10 Gyr. Hence the asteroid belt must have been depleted to near its current mass very soon after asteroid formation. Morbidelli et al. (21) calculate that the asteroid belt could have lost only 1/3 of its current mass over a 10 Gyr equivalent of its present collisional activity. This low level of collisional grinding implies that the current size distribution of asteroids larger than 60 km in radius is primordial (20).

The formation of embryos in the asteroid belt provides a means to excite the smaller asteroids to their current, high eccentricities (25). Embryos can also be responsible for the rapid clearing of the asteroid belt, since asteroids are gravitationally scattered by the embryos and hence move readily to resonances with Jupiter from which they are removed from the belt (76). Hence the



formation of planetary embryos in our chondrule accretion model is completely consistent with mechanisms for depletion of the asteroid belt.

The main alternatives to the embryo model for asteroid belt depletion are (i) sweeping resonances (26) and (ii) the migration of Jupiter in the Grand Tack model (27). The migration of Jupiter and Saturn during the restructuring of the giant planets to their current orbits by scattering of the primordial Kuiper belt leads to a sweeping of resonant locations across the asteroid belt. This could have led to the loss of 90-95% of the mass of the asteroid belt during the migration period (26). The Grand Tack model provides a more violent means for Jupiter's gravity to interfere with the asteroid belt, as Jupiter migrates through the asteroid belt twice; the change from inwards to outwards migration is caused by the formation of Saturn, which comes to share a gap with Jupiter in the protoplanetary disk. This injects C-type asteroids from beyond the ice line into the asteroid belt, which ends up strongly depleted; the later planetesimal-driven migration could inject further icy planetesimals into the main belt (77).

Our simulations show that embryos form readily in the asteroid belt from the accretion of chondrules onto planetesimals. These embryos could have played an important role in sculpting the current orbits of the asteroids and depleting the asteroid belt. There are, as discussed above, mechanisms for the depletion of the asteroid belt that do not require the presence of embryos there. The reality could be that a combination of embedded embryos, sweeping resonances and Jupiter's migration conspired to deplete the asteroid belt to its current mass.